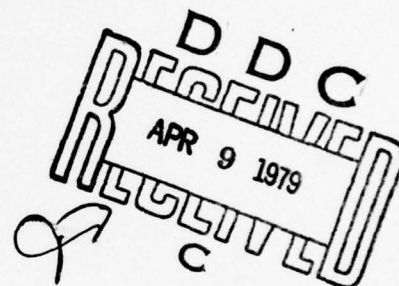END
DATE
FILMED
6-79
DDC

LEVEL 12

Research and Development Technical Report
DAAB07-77-C-2725

AD A067178

HIGH VOLTAGE, LOW INDUCTANCE HYDROGEN THYRATRON STUDY PROGRAM

Robert F. Caristi
David V. Turnquist
EG&G, Inc.
35 Congress Street
Salem, Massachusetts 01970

DDC
RECEIVED
APR 9 1979
C

March 1979

Final Report for the Period 1 October 1977 to 30 September 1978

DDC FILE COPY

Prepared for:
Electronics Technology & Devices Laboratory

ERADCOM

U.S. ARMY ELECTRONICS RESEARCH AND DEVELOPMENT COMMAND,
FORT MONMOUTH, NEW JERSEY 07703

79 04 05 030

HISA-FM 195-78

NOTICES

Disclaimers

The citation of trade names and names of manufacturers in
this report is not to be construed as official Government
endorsement or approval of commercial products or services
referenced herein.

Disposition

Destroy this report when it is no longer needed. Do not
return it to the originator.

REPORT DOCUMENTATION PAGE	READ INSTRUCTIONS BEFORE COMPLETING FORM

1. REPORT NUMBER	2. GOVT ACCESSION NO.	3. RECIPIENT'S CATALOG NUMBER
DELET-TR-77-2725-F	TR-77-2725-F	

4. TITLE (and Subtitle)	5. TYPE OF REPORT & PERIOD COVERED
High Voltage, Low Inductance Hydrogen Thyratron Study Program	Final Report. 1 Oct 77 to 30 Sep 78
	6. PERFORMING ORG. REPORT NUMBER

7. AUTHOR(s)	8. CONTRACT OR GRANT NUMBER(s)
Robert F. Caristi David V. Turnquist	DAAB07-77-C-2725

9. PERFORMING ORGANIZATION NAME AND ADDRESS	10. PROGRAM ELEMENT, PROJECT, TASK AREA & WORK UNIT NUMBERS
EG&G, Inc. 35 Congress Street Salem, MA 01970	62705 1S762705AH94 E1-01 E1

11. CONTROLLING OFFICE NAME AND ADDRESS	12. REPORT DATE
US Army Electronic Technology & Devices Laboratory ATTN: DELET-BG Fort Monmouth, NJ 07703	March 1979
	13. NUMBER OF PAGES
	78

14. MONITORING AGENCY NAME & ADDRESS(if different from Controlling Office)	15. SECURITY CLASS. (of this report)
88 P.	UNCLASSIFIED
	15a. DECLASSIFICATION/DOWNGRADING SCHEDULE

16. DISTRIBUTION STATEMENT (of this Report)

Approved for Public Release; Distribution Unlimited.

17. DISTRIBUTION STATEMENT (of the abstract entered in Block 20, if different from Report)

18. SUPPLEMENTARY NOTES

19. KEY WORDS (Continue on reverse side if necessary and identify by block number)

Thyratron, Switch, Nanosecond Pulser

20. ABSTRACT (Continue on reverse side if necessary and identify by block number)

This report documents the results of a twelve-month study program directed toward gaining the information necessary to fabricate a high voltage, low inductance hydrogen thyratron switch capable of operating with a peak forward anode voltage of 250kV, a peak forward anode current of 20 to 40 kA for 60 ns, and a current risetime of 10 to 20 ns. Operation under these conditions is ultimatley required at high pulse repetition rates.

(over)

DD FORM 1473 EDITION OF 1 NOV 65 IS OBSOLETE
1 JAN 73

390 408

The principal conclusion is that thyratron operation at 250 kV and 40 kA with a current risetime of a few tens of nanoseconds is a feasible proposition. However, the development of a tube having such capabilities is subject to the practical limits that are imposed by the breakdown characteristics of the ceramic insulators that are universally used in the construction of high power tubes. Operation at appreciable repetition rates is clearly subject to the ability of the tube to withstand the heating that results from operation at high average current and high di/dt.

During the first phase of a multi-phase program, the emphasis of the work was placed on those factors that affect the voltage-inductance compromise, since it was determined that the tube's inductance (and not its commutation time) would dominate the maximum achievable di/dt.

It is considered as being clear that a multi-gap tube having an essentially coaxial current return path, and operating with command pulse charging, is required.

The properties of a coaxial geometry, particularly as they apply to the operation of a multi-gap thyratron switch, are discussed at some length. In particular, it is found that the applied voltage is capacitively distributed across the various gaps of the tube, and this phenomenon has significant effects as regards the minimum achievable inductance, and the maximum achievable holdoff characteristics.

It is concluded that experimental work is required to determine the voltage stress capabilities of the ceramic insulators. Ceramic samples have been procured, and a Marx generator has been built and characterized for service as a pulsed, high voltage source for ceramic evaluation tests.

Computer-generated field plots have been used as a design aid, and a mathematical model has been developed for the hydrogen thyratron that accurately predicts the performance of thyratron-switched pulse circuits.

A five-stage tube of a novel, low inductance design has been built to serve as a vehicle for the experimental examination of low-inductance, multi-gap tube operation. The experimental tube is expected to provide information concerning the triggering and commutation characteristics of tightly-baffled, multi-gap structures, as well as their holdoff and recovery properties.

An appendix is included that discusses the mathematical model, and illustrates the technique used to derive the circuit equations that result from the model's use.

TABLE OF CONTENTS

LIST OF ILLUSTRATIONS

-iii-

LIST OF TABLES

1.0 FOREWORD

This Final Technical Report documents the results of a twelve-month study program that commenced 1 October 1977 and ended 30 September 1978, and has generally been known as the High Voltage, Low Inductance Hydrogen Thyratron Study Program. Funded under ERADCOM Contract DAAB07-77-C-2725, this work was directed toward gaining the information necessary to fabricate a thyratron switch capable of operating under the electrical conditions stated in ERADCOM's technical guidelines therefor dated 12 July 1977. The work described herein was performed by EG&G, Inc., Electronic Components Division, 35 Congress Street, Salem, Massachusetts 01970.

The authors of this report wish to recognize specifically the significant contributions made to this Program by Dr. Chathan M. Cooke, Director of Dielectric Research at the High Voltage Research Laboratory, Massachusetts Institute of Technology, and a consultant to EG&G. We wish also to recognize Mr. Jerome J. Hamilton, now with the Raytheon Company, who served as project engineer during the initial phase of the Program.

2.0 INTRODUCTION AND SUMMARY

a. Purpose and Concerns of the Program

The object of the High Voltage, Low Inductance Hydrogen Thyratron Study Program is to obtain the information required to fabricate a thyratron switch capable of operating with the electrical characteristics given in Table 1. This document reports the results of Phase 1 of the Program. As originally contemplated and funded, Phase 1 was to be a study only, with no deliverable hardware. Phase II (now funded under Contract DAAB07-78-C-2977) is wider in scope since the work to be performed consists of further theoretical studies supported and guided by the construction and evaluation of experimental tubes and such other laboratory work as may be deemed expedient.

Table 1. Electrical characteristics for high voltage, low inductance hydrogen thyratron.*

Characteristic	Symbol	Objective
Peak Forward Voltage	epy	250 kV
Peak Anode Current	ib	20 kA**
Pulse Width (90%)	tp	60 nS
Pulse Rise Time (10% to 90%)	tr	5 nS
Current Rate of Rise (10% to 90%)	di/dt	3×10^{12} A/S
Number of Pulses per Burst	—	100
Off Time to Burst Duration Ratio	—	100:1
Total Inductance (Switch and Connectors)	L_T	125 nH

*Table 1 is taken directly from the technical guidelines issued by ERADCOM on 12 July 1977. It is noted that the total inductance and the rate of current rise are not consistent with a peak forward anode voltage of 250 kV. The maximum permissible inductance is calculated elsewhere in this report.

**For tube operation with a Blumlein circuit, the peak forward anode current is 40 kA.

The final electrical requirements for the switch may differ somewhat from those shown in Table 1, but representative characteristics are indeed a peak forward anode voltage of 250 kV, a peak anode current of 20 to 40 kA for 60 nS, a current rise time of 10 to 20 nS, and ultimately, operation at high pulse repetition rates. Figure 1(a) shows the regime of concern of Ib, tr, and di/dt. The current-rise time points shown in Figure 1(a) indicate the region of specific interest. Figure 1(b) shows the total circuit inductance corresponding to the curves of Figure 1(a). The required inductance is seen to be of the order of 30 to 60 nH.
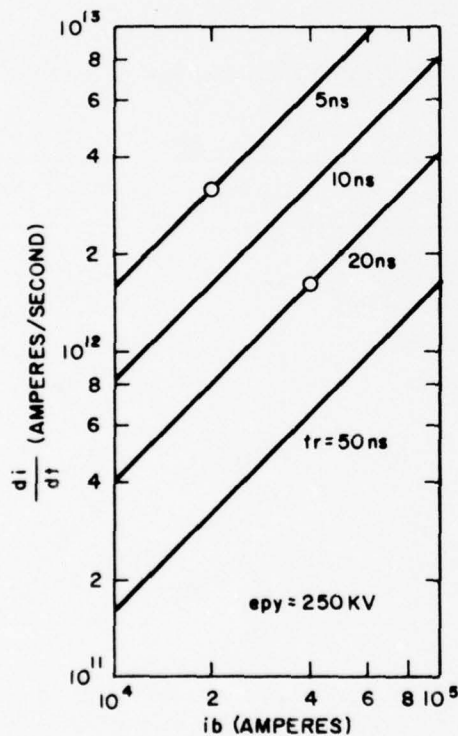
(a)
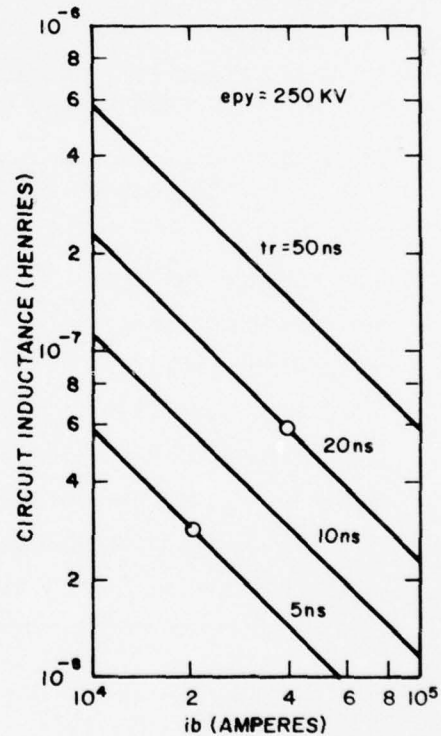
(b)

Figure 1. Regime of peak current (ib), rise time (tr), and di/dt under investigation. A peak current of 40 kA with a rise time of 20 nS is considered feasible.

-4-

No thyratron presently exists that can meet all of these requirements simultaneously, and the performance of existing tube designs cannot be extrapolated to such operating conditions. It is clear that a thyratron capable of meeting the stated requirements can be built only after considerable applied research has been conducted in several areas basic to thyratron technology.

The most fundamental concern germane to this Program is that high voltage and low inductance are, in general, conflicting requirements. Fortunately, the conflict springs from practical concerns such as the properties of insulators, and does not arise from any limitations imposed by basic physics. Therefore, it is subject to resolution by applied research and high voltage engineering.

The effects on thyratron performance of operation at high plate breakdown factors and high rates of current rise are second in importance only to the voltage/inductance compromise. It is difficult to think of any aspect of tube performance and reliability that is not adversely affected by high di/dt at high pulse repetition rates, and such limitations as may be imposed by the constraints of basic physics are apt to lie in this area.

This program has benefited materially from work being done at EG&G under our contract to Los Alamos Scientific Laboratory (LASL).* LASL's requirements for di/dt and tr are substantially the same as those of this Program, and the results obtained under the auspices of either Program are in general useful to the other. An early decision was made to address matters relating to high voltage principally under this Program, and matters relating to di/dt principally under the LASL Program, at least for the first year's effort.

b.   Report Organization and Summary

The work of Phase I has been concentrated on defining the fundamental design concepts that apply to the development of high voltage, low inductance hydrogen thyratrons. The emphasis was placed on the voltage-inductance compromise, with matters pertaining to discharge phenomena and anode dissipation being principally addressed under our contract to LASL.

---

*Contract No. EN-77-C-04-4047.

In Section 3 of this report, the basic aspects of low inductance tube design are discussed. The limitations placed on the achievable di/dt by the commutation properties of the tube and by the total circuit inductance are considered in depth. We conclude that the operating conditions pertinent to this Program correspond to a point near the borderline of the two effects, but that the circuit inductance is still the more significant concern. Ignoring temporarily the matter of voltage stress, we conclude that a hydrogen thyratron capable of operating at 40 kA with a rise time of 20 nS is in fact a feasible proposition.

The following parts of Section 3 address the more obvious characteristics of a high voltage, low inductance tube such as multi-gap construction, the requirement for command pulse charging, and the clearly heavy stresses imposed on the tube's insulating sections by the need for physical shortness. Consideration is then given to the need for a coaxial geometry, for which inductance, stray capacitance, and voltage stress are investigated. As one would expect, minimum inductance is achievable only at the expense of increased stray capacitance and increased voltage stress.

To establish an optimized design, the realities imposed by practical methods of thyratron construction must be considered. This is done in Section 4. First, the maximum permissible inductance consistent with 40 kA rising in 20 nS is calculated; this inductance was found to be somewhat less than 60 nH. Then, the physical dimensions and construction of practical multi-gap tubes are addressed and the importance of the stray capacitance between the tube's various electrodes and the coaxial current return is established. The effect of the strays is to "short-out" the lower gaps such that an ever larger fraction of the applied charging voltage appears across the uppermost gaps. This phenomenon establishes a point of diminishing return insofar as the number of gaps is concerned, and the optimum number of stages is thus calculable as a function of the ratio of the interelectrode capacitance to the stage's stray capacitance to ground. The conclusion is drawn that the optimum number of stages is typically four to six for anticipated capacitance ratios, which number is the minimum consistent with fast pulse charging at 250 kV.

-6-

In Section 4, the complex interaction of the various parameters pertinent to the design is discussed, and some simplifying but justified assumptions are made to eliminate some variables and thus bound the problem. It is concluded that oil is the preferred medium for insulating the tube with respect to its coaxial current return, and also that it is desirable to design the return so as to utilize the maximum available space. The triggerability-holdoff compromise is considered briefly, but extensive practical experience tells us that holdoff will be the more pressing concern.

Finally in Section 4, consideration is given to the need for experimental work to determine the stress levels that high-purity alumina will withstand under pulsed conditions. This information is not otherwise available, and such knowledge is vital to the design of a viable tube. The ceramic samples that we intend to test are discussed briefly, and the 250 kV Marx generator that we have built and characterized to serve as a pulsed high voltage source for sample testing is also described.

Section 5 presents a discussion of some of the additional theoretical work that we have performed during Phase I and that will be of continued assistance to us during Phase II. The use of computer-generated field plots as a design aid is described and representative plots are included by way of example. Field plotting will be of particular value during Phase II as a tool to aid us in performing an in-depth theoretical study of the triggerability-holdoff compromise.

Section 5 also discusses a mathematical model that we have developed for the hydrogen thyratron. This model accurately predicts tube and circuit behavior under a variety of operating conditions, and enables us to perform on paper valuable parametric studies that would be prohibitively expensive and time consuming if performed in the laboratory. As an illustrative example, experimental data are compared with the tube's performance as predicted by the model for a thyratron operated under both high and low conditions of di/dt. The results are highly consistent, and reveal the probable phenomenon of a time-varying tube inductance (or resistance) during the early portion of the anode current pulse. This is a likely occurrence of as yet unknown impact, and it is subject to further theoretical and experimental study.

In Section 6, the first experimental high voltage, low inductance hydrogen thyratron to be designed under the Program is described. The need for a full-scale experimental device is addressed first, followed by a discussion of the overall philosophy that guided our design. Finally, the various aspects of the design are examined in detail.

Section 7 presents the principal conclusions that we have reached as a result of our work during Phase I and describes our plan for future work under Phase II. By far, the most important conclusion is that a hydrogen thyratron capable of operation at 250 kV and 40 kA with a current rise time of a few tens of nanoseconds is a feasible proposition. It is nonetheless clear that the successful development of such a switch requires considerable finesse, and is subject to the practical limits imposed by the breakdown properties of insulators and (at any appreciable pulse repetition rate) the ability of the structure to withstand the heating resulting from high average current and high di/dt.

The references cited in this report are listed in Section 8. Also included (as an Appendix) is a description of our mathematical model for the hydrogen thyratron, together with a discussion of the technique that we used to establish the equations pertinent to the operation of thyratron-switched pulse circuits.

3.0 BASIC ASPECTS OF HIGH VOLTAGE, LOW INDUCTANCE TUBE DESIGN

a. Commutation and Inductance Limitations on di/dt

Figure 2 shows the "resistive" fall time (total closure time) as a function of operating pressure for a variety of high voltage gas discharge switches. The term "resistive" means that the anode fall times shown were observed under conditions of relatively slow di/dt such that no significant voltage drop occurred across the inductance inherent in the switch. The data shown are empirically determined, but the trend in evidence in Figure 2 covers an impressively wide range of fall time and pressure.

From Figure 2 one can calculate a mean (geometric) operating pressure and a mean fall time for each of the switches shown. The results of this calculation appear in Table 2.

Table 2. Mean pressure and mean fall time for various gas discharge switches.

Switch	Pressure Range (Torr)	Total Fall Time Range	Mean Pressure (Torr)	Mean Total Fall Time, T
LMPV*	$10^{-6} - 10^{-5}$	2-5 µS	3.16×10^{-6}	3.16 µS
Vacuum Gap	$10^{-4} - 8 \times 10^{-3}$	250-500 nS	8.94×10^{-4}	354 nS
CFCS**	0.1	30-50 nS	0.1	38.7 nS
Hydrogen Thyratron	0.2-1	10-50 nS	0.447	22.4 nS
Krytron	10	2 nS	10	2 nS
Spark Gap	800 - 1000	0.5-2 nS	890	1 nS

*Liquid Metal Plasma Valve

**Crossed Field Closing Switch
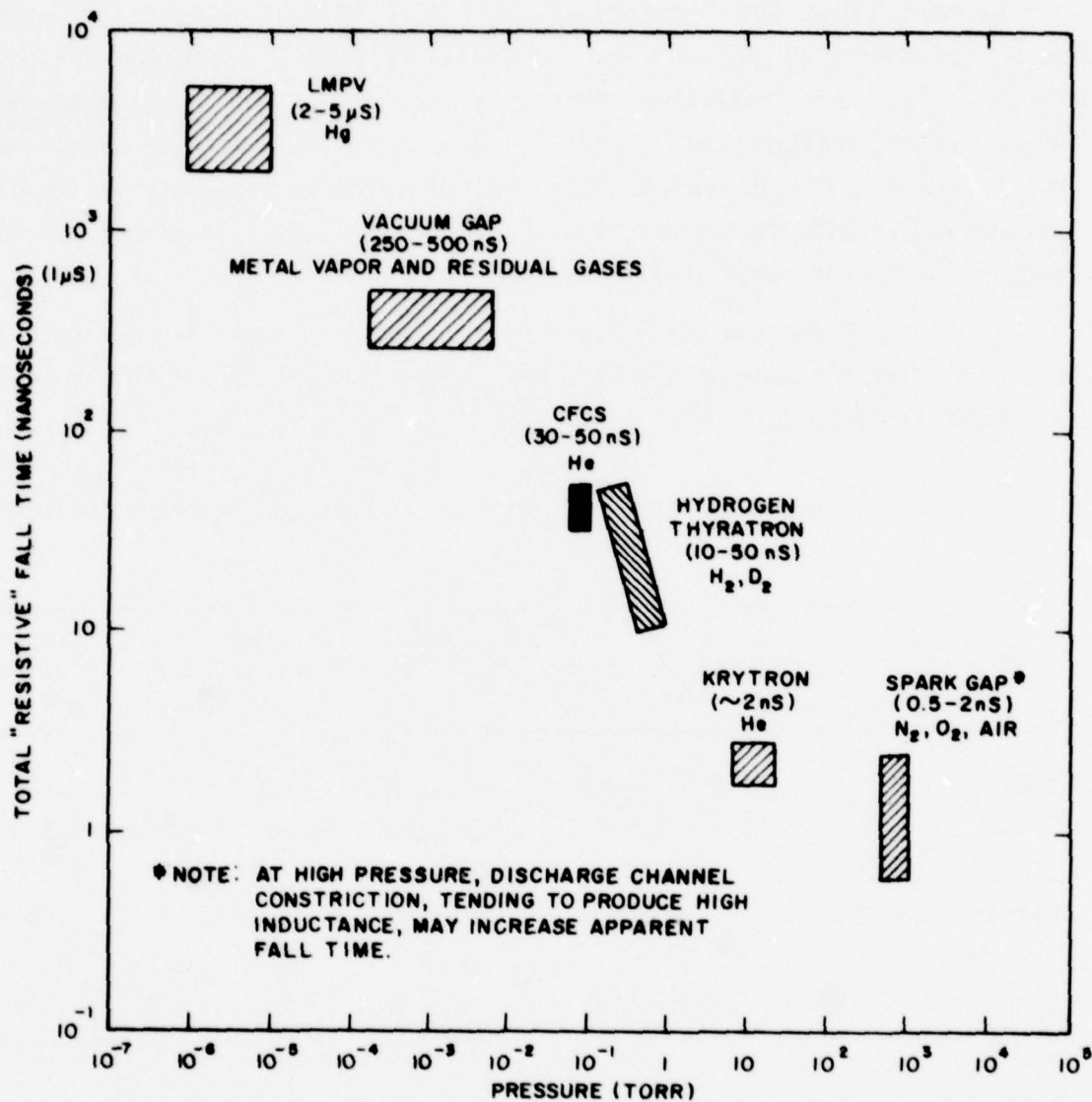
Figure 2. "Resistive" fall time (closure time) as a function of operating pressure for various gas discharge switches. The map was generated from empirical data and covers an impressive range of pressure and fall time.

It will be shown later in this report that the "resistive" anode fall of a hydrogen thyratron can be characterized by an ionization time constant, τ_i, which depends only on gas pressure and is defined by the relation $\tau_i = T/\ln 2$, where T is the resistive fall time of the tube. Extending this procedure to the mean fall times shown for each switch in Table 2, one can establish the curve of Figure 3, which relates the ionization time constant to the operating pressure.

For a circuit operating with zero inductance, the current would rise in the same manner as the anode fell. We have developed a model for the hydrogen thyratron which gives the normalized instantaneous anode potential during commutation as $e(t)/V_0 = 2 - \epsilon^{t/\tau_i}$. For a purely resistive circuit, the normalized current as a function of time would then be $i(t)/I_0 = \epsilon^{t/\tau_i} - 1$ where I_0 is the peak current. Solving this equation for the 10% point, we find $t_{10} = 0.095 \tau_i$. Solving for the 90% point, we find $t_{90} = 0.642 \tau_i$. Subtracting these times gives $tr = 0.547 \tau_i$. The excursion of $i(t)$ during this time interval is $0.8 I_0$ (amperes). The slope of a line through these points is $di/dt = 0.8 I_0/0.547 \tau_i$ (amperes/second) or $1.46/\tau_i$ (amperes/sec/volt).

A similar exercise can be performed for an inductive circuit where $e(t) = 0$; i.e., for a perfect switch, such that the rise time is then limited only by the circuit inductance. This yields $di/dt = 0.363/L$ (amperes/sec/volt). Combining both the commutation and the inductive effects yields the map of Figure 4.

The region of high di/dt and low pressure in Figure 4 is not accessible because no switch is known to exist that operates in this region. Similarly, the regime corresponding to sub-nanohenry operation is the exclusive domain of the high pressure spark gap. Note that the intersection of a given inductance with a given switch does not necessarily mean that the switch has such an inductance. The intersection in fact means that the commutation time of the switch would limit tr to the same value as would the intersecting inductance.
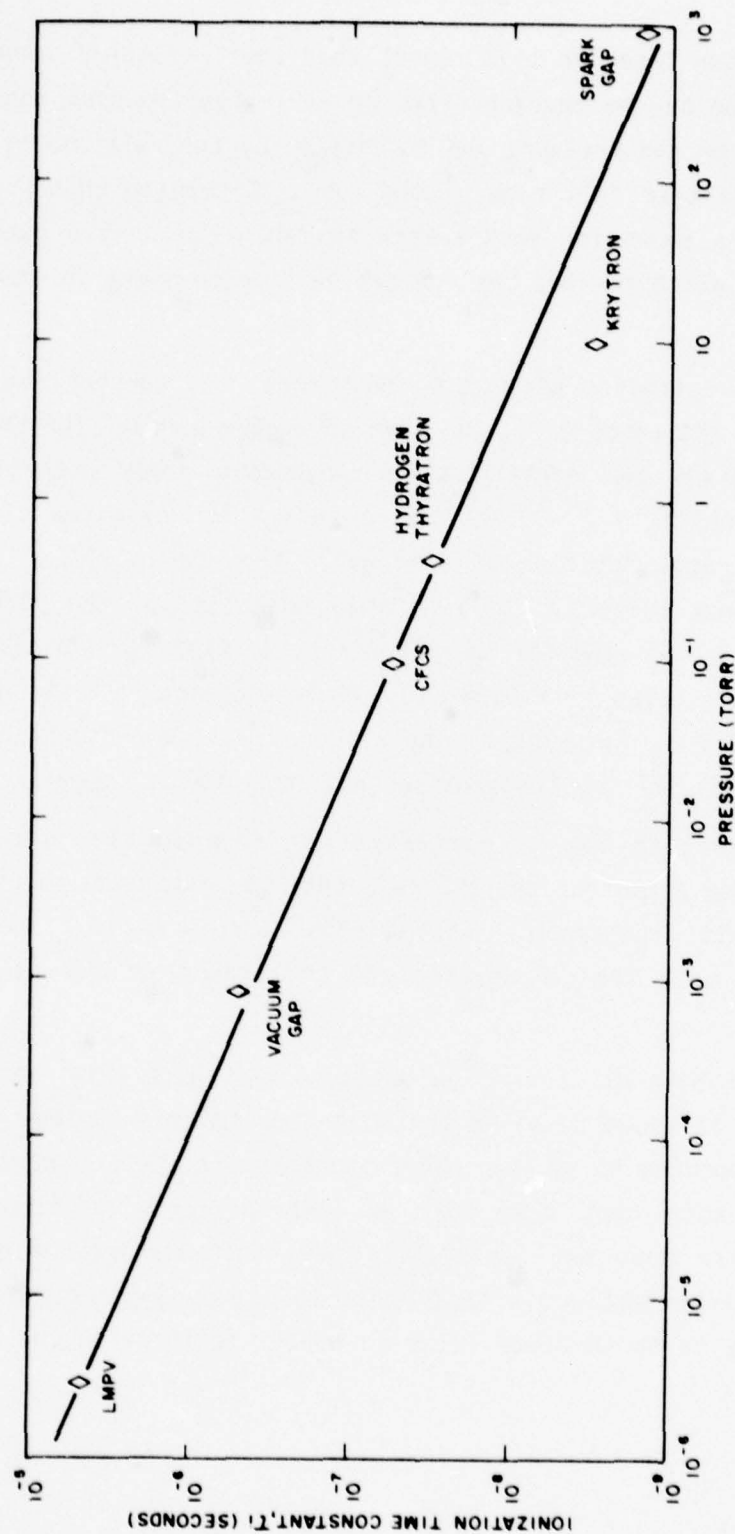
Figure 3. "Ionization" (closure) time constants as a function of operating pressure for various gas discharge switches. The values shown represent the geometric mean of the ranges indicated in Figure 2.

-12-
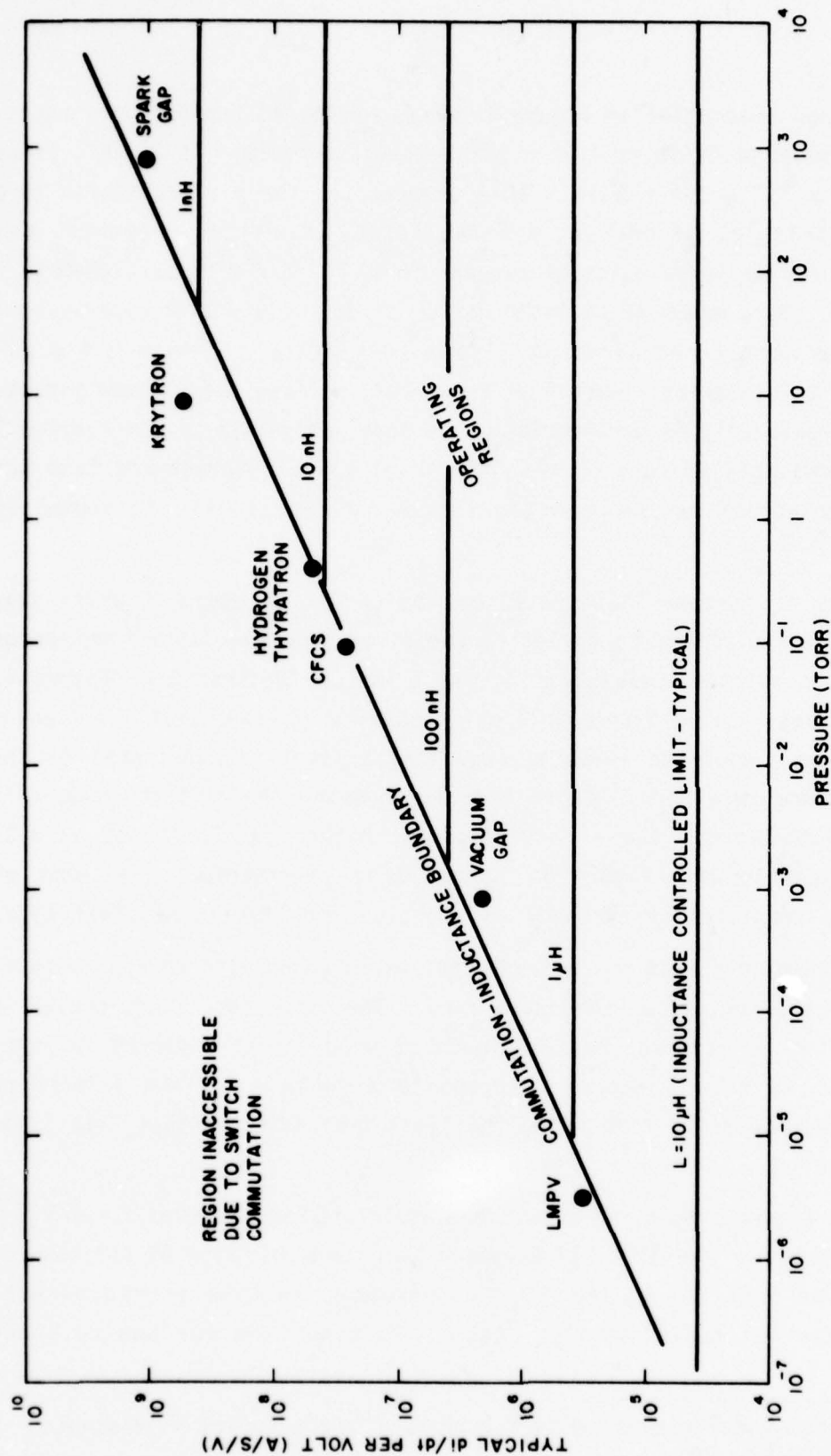
Figure 4. Limits imposed on di/dt per volt due to commutation effects and circuit inductance. For the operating conditions pertinent to this program, the normalized di/dt per volt is 6.4 x 10⁶, which implies a total circuit inductance of somewhat less than 60 nH. For a hydrogen thyratron switch, the circuit is inductance-controlled.

-13-

Consider now that point in Figure 4 corresponding to the hydrogen thyratron. The normalized di/dt is 4.56×10^7 amperes/sec/volt. At 250 kV, di/dt is $4.56 \times 10^7 \times 250 \times 10^3 = 1.14 \times 10^{13}$ amperes/sec for a circuit with zero inductance. This is, of course, not realistic. Consider, however, the pertinent requirement for a pulse of current of 40 kA peak with tr (10%-90%) = 20 nanoseconds. This means 32 kA in 20 nS, or di/dt = 1.6×10^{12} amperes/sec. At 250 kV, the normalized di/dt is $(1.6 \times 10^{12})/(250 \times 10^3) = 6.4 \times 10^6$ amperes/sec/volt. Entering Figure 4 at 6.4×10^6, we find the maximum inductance to be approximately 60 nanohenries. (We later calculate 57 nanohenries.) It is clear from this discussion that the total circuit inductance (and not thyratron commutation) can be expected to dominate di/dt for the regime of interest.

This point is further illustrated by the curves of Figure 5 which show the results of calculations to determine the circuit current as a function of time for various hypothetical operating conditions.* Referring to Figure 5, observe the curves labeled 1 through 3 which show the current that would ensue as the thyratron commutated (with various ionization time constants) if the circuit inductance were zero. Curve 1 corresponds to the fastest anode fall time generally observed. Curve 3 corresponds to the mean fall time as discussed in connection with Figure 3. Curve 2 is representative of what we believe can be consistently achieved in practice for "resistive" fall time.

Curves 4 through 6 show the current that would ensue with various circuit inductances if the ionization time were zero. The inductance range chosen is representative of our current best estimate of what can be achieved in practice for a 250 kV tube. Curves 7 through 9 show the combined effects of inductance and commutation time using the ionization time constant that seems most reasonable.

Note from Figure 5 that the rise times associated with Curves 7 through 9 do not differ greatly from those of Curves 4 through 6 in spite of the assumed ionization time constant of 20 nS. The commutation time serves more to "delay" the current pulse than to change its rise time for the relative

---

*The mathematical model used to generate most of these curves is discussed in Appendix 1 to this report.

-14-

CURVE NO.	L(nH)	T_L(nS)	T_i(nS)	t_r(nS)
1	0	0	14.4	7.89
2	0	0	20.0	10.9
3	0	0	32.3	17.6
4	40	6.4	0	14.1
5	60	9.6	0	21.1
6	80	12.8	0	28.1
7	40	6.4	20	18.4
8#	60	9.6	20	24.8
9	80	12.8	20	30.5

MOST PROBABLE OPERATING CONDITIONS

NORMALIZED CURRENT

TIME (NANOSECONDS)
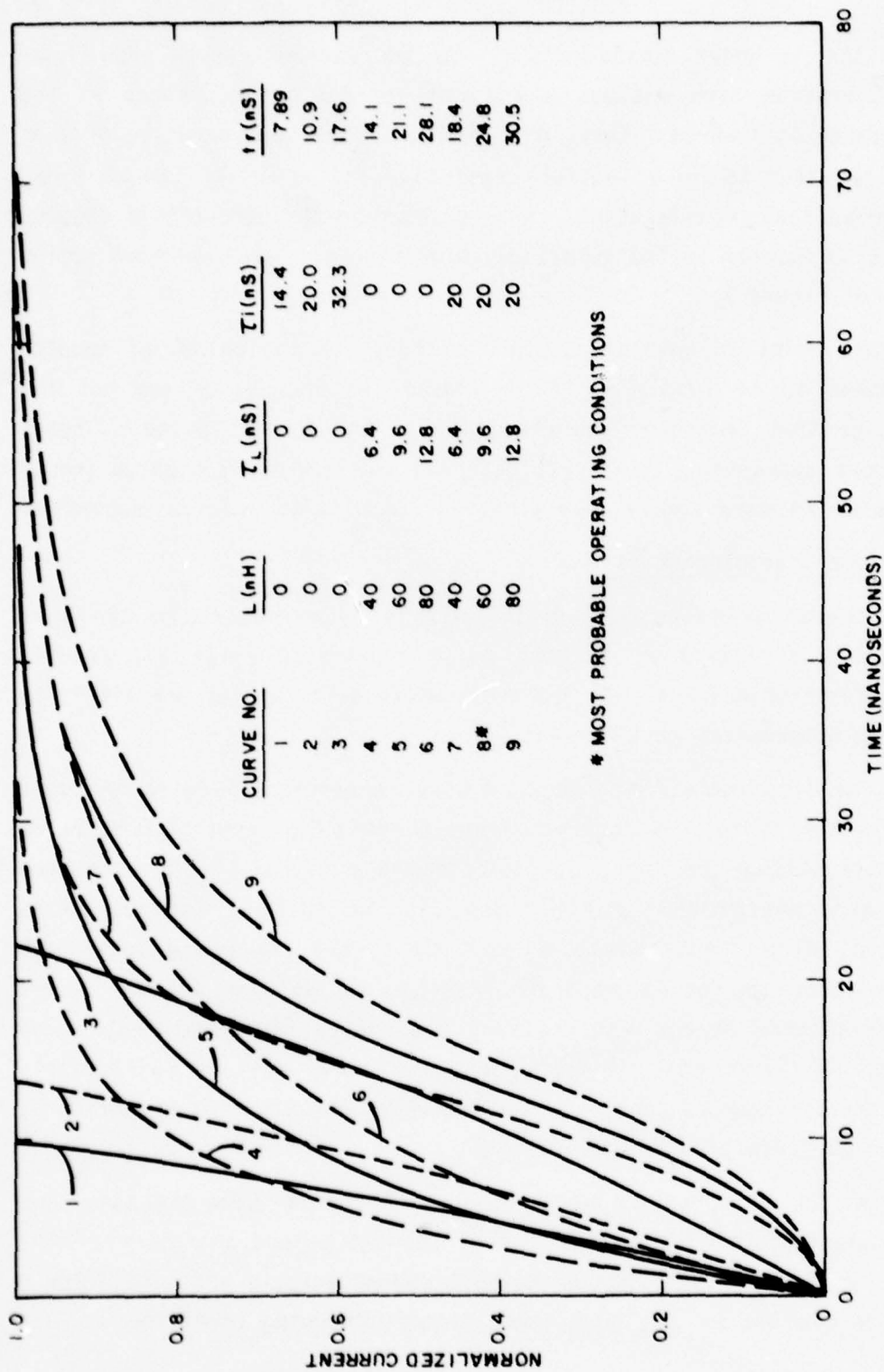
Figure 5. Calculated current as a function of time for various hypothetical operating conditions. Curves 1, 2, and 3 assume a finite commutation time and zero inductance. Curves 4, 5, and 6 assume a zero commutation time and various circuit inductances. Curves 7, 8, and 9 show the combined effects of commutation time and inductance.

values of τ_L and τ_i under consideration. As the various curves show, however, the commutation time assumes a role of increasing importance as the circuit inductance is lowered. Curve 8 is perhaps most representative of what we presently consider to be a feasible rise time for a 250 kV, 40 kA tube, subject to the various considerations that we describe throughout this report. We thus expect to operate in the relatively high current, low rise time region of the curves of Figure 1.

The overall point of this discussion is that, for the values of inductance that appear to be feasible, it is indeed the inductance and not the commutation time that dominates the rise time of the current pulse. Therefore, it is more appropriate to investigate ways of achieving minimum inductance as opposed to extensively investigating commutation related phenomena.

b.   Obvious Tube Characteristics

Several characteristics of a high voltage, low inductance hydrogen thyratron capable of operation at high pulse repetition rates are readily apparent from first principles. So are areas where difficulties are likely to arise and where compromises must be made.

To keep the inductance low, the tube must be physically short and must operate with a coaxial current return. To hold off a high epy, it must be of multi-gap construction. As such, it must contain a plurality of short (and not nested) gradient grids. Furthermore, it should be triggered by an auxiliary grid, with a negative bias applied to the control grid. Such triggering promotes the development of a dense and uniform plasma in the auxiliary grid-cathode space, which plasma eventually penetrates into (and thus triggers) the first gap. Finally, all electrodes must be sufficiently massive to withstand (and conduct) the heating which results from operation at high prr and high di/dt.

High di/dt implies operation at the highest practical tube pressure, but this is inconsistent with high epy. Hence, command pulsed charging is mandated to take advantage of the higher holdoff characteristic achievable for a given electrode spacing and pressure under dynamic charging conditions. This

-16-

implies that epy will be distributed across the various gaps in inverse proportion to the gap capacitances. But the effective capacitance for voltage division purposes is a function of the capacitance to ground. Thus the grid-to-ground capacitance is a factor of importance.

The requirement for shortness imposes heavy voltage stress on the inter-grid spacers during the charging cycle. This problem is compounded during the cascading process, as an ever-increasing fraction of epy appears across the last gaps to break down until finally the full voltage epy appears across the last unfired gap. Heavy stress is also placed on the insulating medium which fills the space between the tube and its grounded current return. Not only must there be no breakdown between any of the tube's electrodes and ground, there must also be no breakdown between adjacent grids during the charging period.

c. Properties of a Coaxial Geometry*

(1) Inductance

The complete solution for the low frequency** inductance, L, per unit length, d, of a structure containing no magnetic material, and comprised of infinitely long, smooth coaxial cylinders*** having finite cross-sectional areas is [1]

$$\frac{L}{d} = \mu_o \left\{ \frac{1}{8\pi} + \frac{1}{2\pi} \ln \frac{b}{a} + \frac{1}{2\pi} \left[\frac{c^4}{(c^2 - b^2)^2} \ln \frac{b}{a} - \frac{3c^2 - b^2}{4(c^2 - b^2)} \right] \right\} \quad (1)$$

---

*Throughout this analysis, we will assume that the tube and its coaxial current return path can be treated mathematically as an infinitely long coaxial structure. Such errors as are introduced by this assumption are of a quantifying nature only, and do not diminish the value of the basic principles that are established.

**We temporarily avoid the complications introduced by rapidly time-varying fields.

***We assume that the discharge in the thyratron is basically cylindrical.

where μ_0 is the permeability of free space and the radii a, b, and c are as defined in Figure 6.
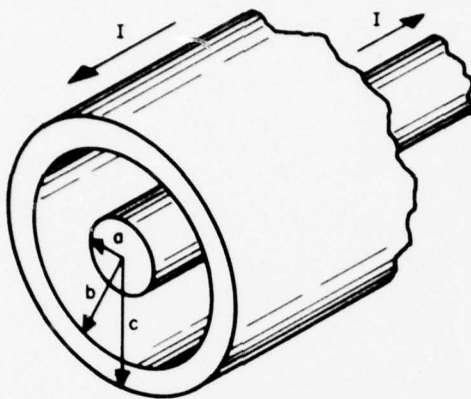
Figure 6. A structure composed of coaxial cylinders of finite dimensions. The inductance is decreased as the thickness of the outer conductor and the annular region between the conductors is decreased, but zero inductance cannot be achieved if the length of the structure is finite. The minimum possible inductance is 1.27 nanohenries per inch.

Rewriting Equation 1,

$$\frac{L}{d} = \frac{\mu_0}{8\pi} + \frac{\mu_0}{2\pi} \ln \frac{b}{a} + \frac{\mu_0}{2\pi} \left[\frac{c^4}{(c^2 - b^2)^2} \ln \frac{b}{a} - \frac{3c^2 - b^2}{4(c^2 - b^2)} \right] \tag{2}$$

or

$$\frac{L}{d} \equiv L_1 + L_2 + L_3 \tag{3}$$

Note that the term L_1 is independent of the radii. As such, it establishes an absolute minimum low-frequency inductance for the structure which is simply

$$L_1 = \frac{\mu_o}{8\pi} = \frac{4\pi \times 10^{-7}}{8\pi} = 50 \ nH/m$$

or   (4)

$$L_1 = 1.27 \ nH/inch$$

The term L_3 takes into account the magnetic field energy present in the volume per unit length of the outer conductor. This term becomes negligibly small as c approaches b; i.e., as the thickness of the current return approaches zero. A thin return is easily accomplished in practice and is mandated at high frequencies by the "skin effect" phenomenon.* Even if the skin effect did not apply, one might assume a current return thickness of 0.125 inch. The inductance associated with this thickness (assuming c = 7 inches) is L_3 = 0.031 nH/inch which is about two percent of L_1 and small by any standard. We therefore neglect the contribution of this term.

Consider now the term L_2 which may be written

$$L_2 = \frac{\mu_o}{2\pi} \ ln \ \frac{b}{a} = \frac{4\pi \times 10^{-7}}{2\pi} \ ln \ \frac{b}{a}$$

or   (5)

$$L_2 = 5.08 \ ln \ \frac{b}{a} \ nH/inch$$

This term is based on the magnetic field energy in the annular region between the conductors and is of course the term of prime concern to this Program.

---

*For a single pulse of 60 nS duration, the frequency of the fundamental is 16.7 mHz. For a copper return (conductivity 5.8×10^7 mhos/m), the $1/\epsilon$ depth is only 0.64 mil. The skin effect is probably not relevant to the thyratron discharge itself, where the conductivity is relatively low. The use of Equation 4 is thus in order.

Combining Equations 3, 4, and 5 we write

$$\frac{L}{d} = 1.27 + 5.08 \ln \frac{b}{a} \quad \text{nH/inch} \tag{6}$$

A plot of Equation 6 is shown in Figure 7. Note that the second term domi-
nates the total inductance until the ratio b/a approaches unity. The two
terms are equal at b/a = 1.284.

(2) Capacitance

The capacitance, c, per unit length, d, for a coaxial structure*
is (2)

$$\frac{c}{d} = \frac{2\pi\varepsilon}{\ln \frac{b}{a}} \tag{7}$$

where b and a are as defined in Figure 6 and ε is the permittivity of the
medium between the radii b and a.** For a medium of relative permittivity ε_r,
Equation 7 may be written

$$\frac{c}{d} = 1.412 \ \varepsilon_r / \ln \frac{b}{a} \quad \text{pF/inch} \tag{8}$$

(3) Maximum Stress

The general relation for the maximum voltage stress in the region
between smooth*** coaxial cylinders is (3)

---

*We temporarily assume that the thyratron can be considered as a smooth-
walled cylinder. This avoids the complications due to grid flanges and
guard rings.

**The permittivity is usually expressed as $\varepsilon = \varepsilon_0 \ \varepsilon_r$ where ε_0 is the permitti-
vity of free space (8.85×10^{-12} farads/meter). For vacuum and most
gases, $\varepsilon_r = 1$; for most oils, $\varepsilon_r = 2$ to 3; for water, $\varepsilon_r = 80$.

***A deviation from smoothness will increase the maximum stress as discussed
further below.
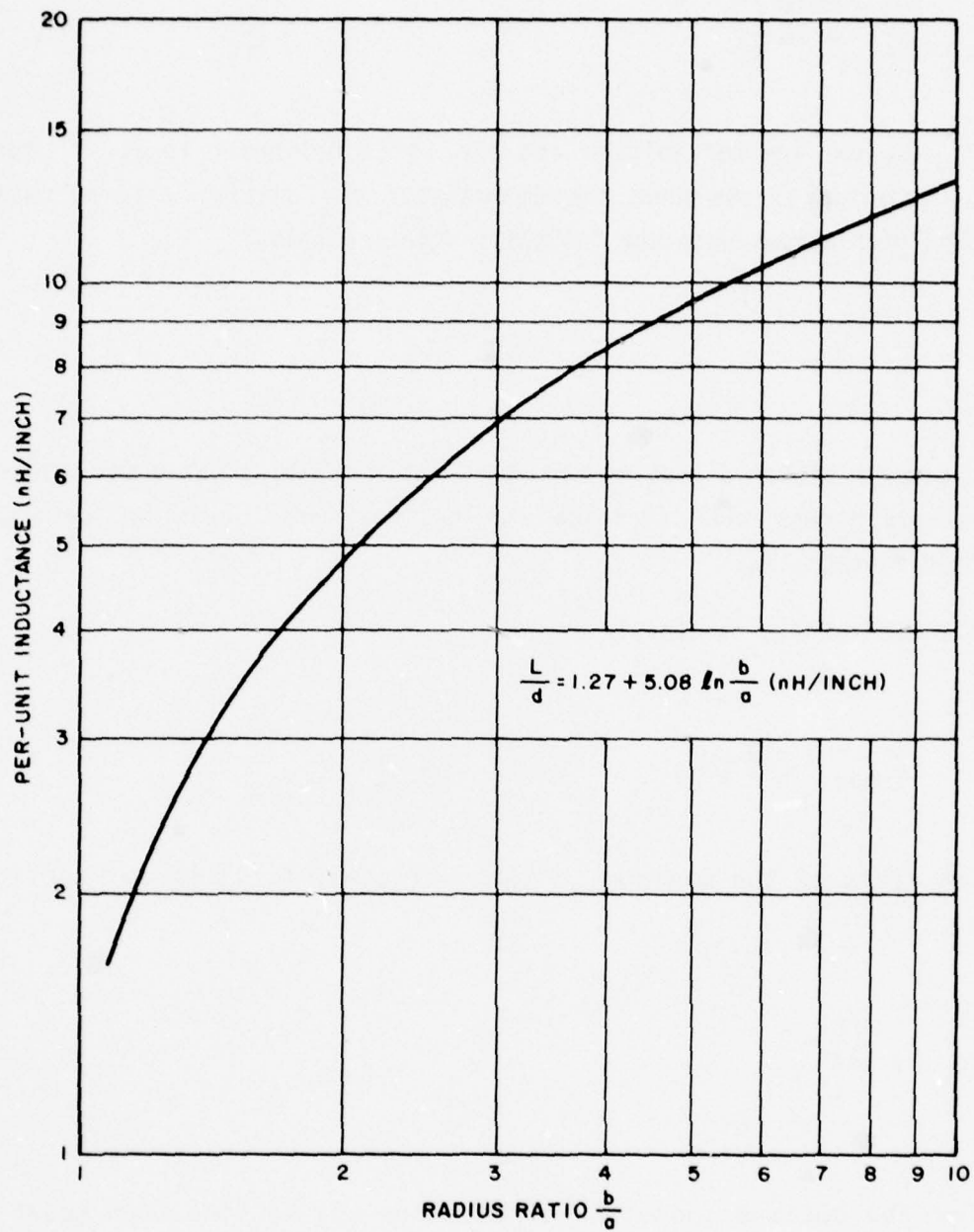
Figure 7. Inductance per unit length as a function of the radius ratio, b/a. At b/a equal to unity, the inductance is 1.27 nanohenries per inch.

$$Em = \frac{V_o}{a \ln \frac{b}{a}} \tag{9}$$

where V_o is the applied voltage and b/a is as defined before. An optimum stress condition exists when the denominator of Equation 9 is at maximum. This condition arises when the following relation holds:

$$\frac{b}{a} = \varepsilon \tag{10}$$

A departure in either direction from this optimum radius ratio for minimizing the maximum stress will increase the gradient and lower the permissible operating voltage, V_o.

The mean stress is clearly

$$E_{mean} = \frac{V_o}{b - a} \tag{11}$$

and the ratio of the maximum to mean stresses, f, is (from Equations 9 and 11)

$$f = \frac{\left(\frac{b}{a}\right) - 1}{\ln \frac{b}{a}} \tag{12}$$

For the optimum condition of Equation 10, we find from Equation 12

$$f_{optimum} = \varepsilon - 1 = 1.72 \tag{13}$$

i.e., even under the best of conditions, the maximum stress is nearly twice that for plane-parallel electrodes.

-22-

Deviations from smoothness (as occur when flanges and guard rings are used on a thyratron) serve to increase the maximum stress. Consider the stress in the region between two infinite plane-parallel plates spaced apart by a dimension a. The maximum stress is clearly V_0/a where V_0 is the applied voltage as before. Now consider the situation depicted in Figure 8 where a semi-cylindrical "bump" of radius r has been added to one of the plates. The maximum stress is then[4] $2V_0/a$ even though $a \gg r$.
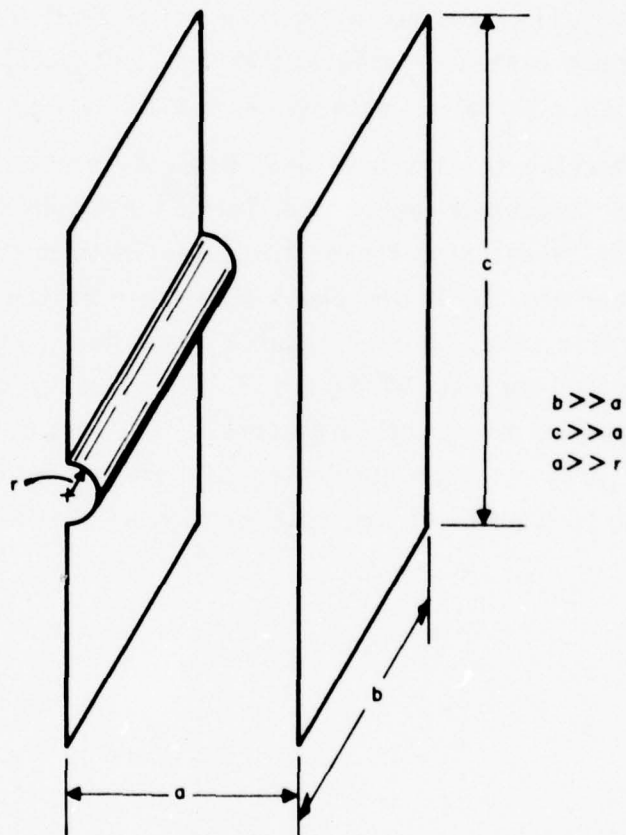
Figure 8. A geometry chosen to illustrate the field effects of small perturbations in electrode geometry. The small, semicylindrical "bump" doubles the maximum stress in the region between the plates.

(4) Summary

From Equations 6, 8, and 9, one can develop a family of curves for L/d, C/d, and Em as a function of the radius ratio, b/a. L/d depends only on b/a since only nonmagnetic materials need be considered. C/d depends both on b/a and the relative permittivity, ε_r. Em depends on b/a, the value chosen for b (or a), and the applied voltage, V_0. Such curves are shown in Figure 9, where C/d has been calculated for ε_r = 1, 2, and 3, and Em has been calculated for Vo = 250 kV, and b = 7, 6, and 5 inches. The range chosen for ε_r is appropriate for most insulating oils and gases. The range chosen for b includes the maximum dimension consistent with the needs of this Program (14-inch diameter) and, at the low end, about the minimum dimension consistent with a thyratron cathode capable of delivering 40 kA.

Referring to Figure 9, one observes several points worthy of note. Reducing the inductance below the level corresponding to the minimum Em (6.45 nH/inch) causes significant increases in both stress and stray capacitance. Furthermore, these increases accelerate as the inductance is reduced. At a given ratio, b/a, Em is of course lower for a larger b. Exactly where one operates on the map of Figure 9 is obviously determined by the best overall compromise among the parameters b, ε_r, and d; i.e., that solution to the overall problem that satisfies all of the boundary conditions. We address these boundaries in the next section of this report.
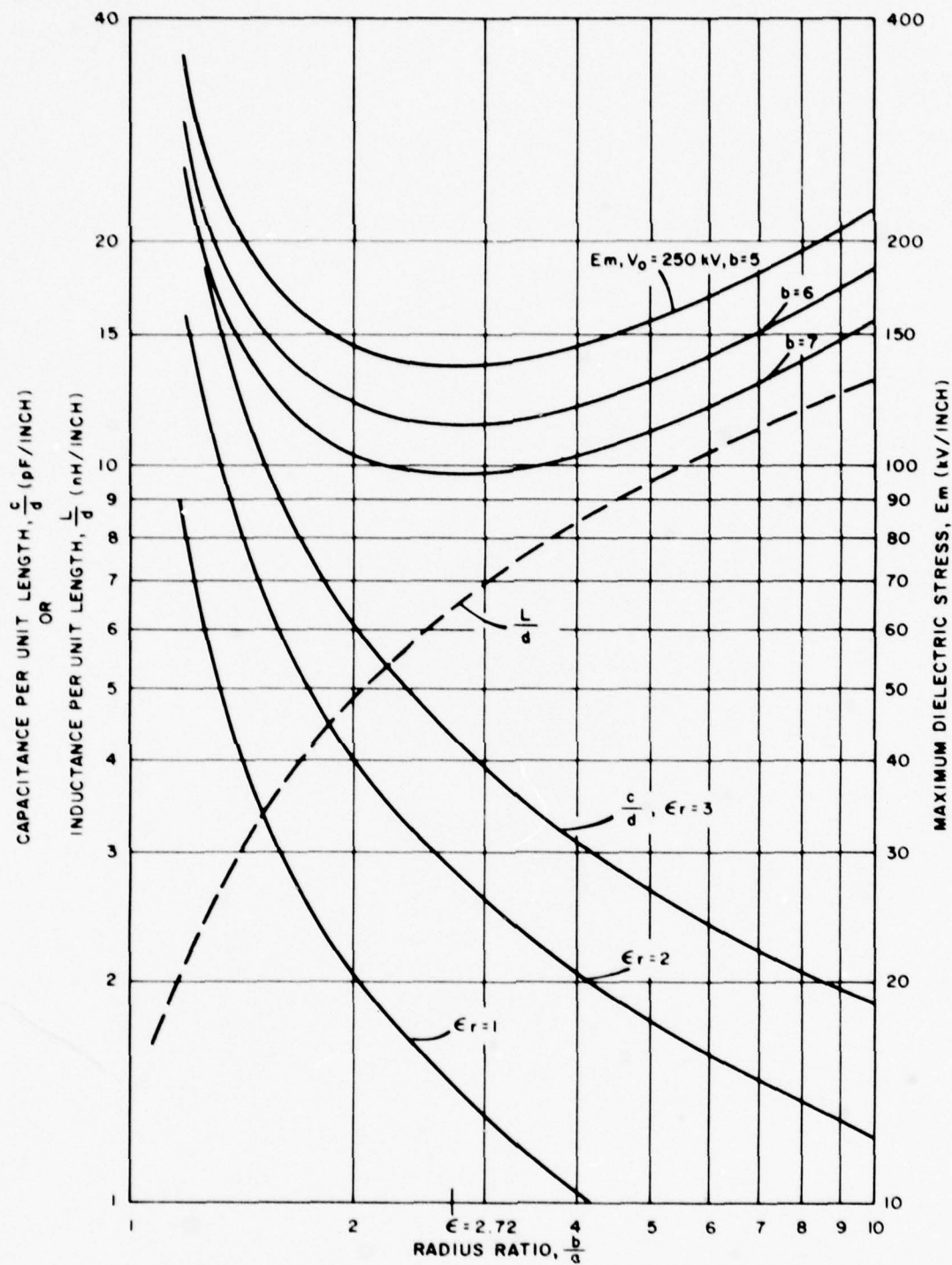
Figure 9. Inductance, capacitance, and maximum stress for coaxial cylinders as a function of the radius ratio, b/a. The capacitance is directly proportional to the permittivity of the medium between the cylinders. The maximum stress varies inversely with the dimensions of the structure, and is at a minimum when b/a = ε = 2.72.

4.0 DESIGN OF A PRACTICAL TUBE

a. Maximum Permissible Inductance

In Section 3 we argued that tube inductance (and not anode fall time) would dominate the current rise time. Our experimental work supports this conclusion as do the results we obtain using a mathematical model we have developed for the tube. We therefore begin our discussion of tube design by calculating the maximum permissible tube inductance, L_T (max), on the assumption that L_T dominates the total circuit inductance.

We assume epy = 250 kV, ib = 40 kA, and tr (10% to 90%) = 20 nS. Clearly, for an inductance-controlled circuit,

$$i(t) = Ib(1 - \varepsilon^{-t/\tau}) \tag{14}$$

where i(t) is the instantaneous tube current and Ib is the peak current. Setting i(t) = 0.1 Ib and solving Equation 14 for t,

$$t(0.1 \text{ Ib}) = 0.105\tau \tag{15}$$

Similarly,

$$t(0.9 \text{ Ib}) = 2.303\tau \tag{16}$$

Then

$$tr = (2.303 - 0.105)\tau \tag{17}$$

Setting tr = 20 nS and solving Equation 17 for τ,

$$\tau = 9.099 \times 10^{-9} \text{ sec} \tag{18}$$

Since

$$\tau = \frac{L_T \text{ (max)}}{R} = \frac{L_T \text{ (max)}}{epy/Ib}$$

then

$$L_T \text{ (max)} = \frac{epy}{Ib} \tau = \frac{250 \times 10^3}{40 \times 10^3} \times 9.099 \times 10^{-9}$$

from which

$$L_T \text{ (max)} = 56.87 \text{ nH} \tag{19}$$

b. Dimensions of a Practical Tube

In the discussion of Section 3, it was tacitly assumed that a single dimension "a" was appropriate for calculations of L/d, C/d, and Em. In practice, this is not so. For inductance calculations, the dimension usually used for "a" is the outer radius of the outer grid slots. This assumes that the discharge has substantially filled the tube by the time the anode current has risen to not more than about ten percent of its peak value. Rough calculations and experimental data support this assumption.

For stress calculations, a different value is appropriate for "a," namely that corresponding to the radius of the grid flanges (and including the guard rings that are necessary to equalize the stress at the external surface of the grid-to-grid spacers). It thus follows that a design optimized for minimum stress between the tube and the current return will of necessity operate with a higher inductance per unit length than that indicated in Figure 9. This augurs for a large diameter tube with propagation of the discharge setting a limit on the diameter.

Still another (and intermediate) value for "a" would seem appropriate for capacitance calculations. This is so because the guard rings do not extend over the full axial length of the tube, and the grid slots are clearly inboard of the equivalent radius for capacitance purposes. It therefore follows that a tube designed for minimum stress will operate with a lower C/d than that indicated by Figure 9.

c. Effects of Stray Capacitance

From Equation 19, we have established the maximum permissible tube inductance as being about 57 nH. This defines L_T (max) but not L/d. Recalling Equation 6,

$$\frac{L}{d} = 1.27 + 5.08 \ln \frac{b}{a} \tag{6}$$

Thus

$$\frac{L}{d} \cdot D = 1.27 D + 5.08 D \ln \frac{b}{a} \tag{20}$$

where D is the effective length of the tube. A curve showing the relation between D and b/a for various values of L_T and including $L_T = 57$ nH is shown in Figure 10.

The effective length, D, is a function of the number of gaps required to hold off epy, and also a function of the required interstage insulator length. The ratio b/a is a function of the maximum allowable stress between "cylinders" and also a function of the effective stage-to-ground capacitance. But the number of gaps and the stray capacitance are also related in that the strays effectively "short-out" the lower stages during the charging cycle, thus forcing the upper gaps to withstand an ever-larger fraction of epy. It is clear that a point of diminishing returns exists as regards the number of gaps. To determine this point, we must make some assumptions regarding an optimized design. We must, in effect, "get into the ball park."
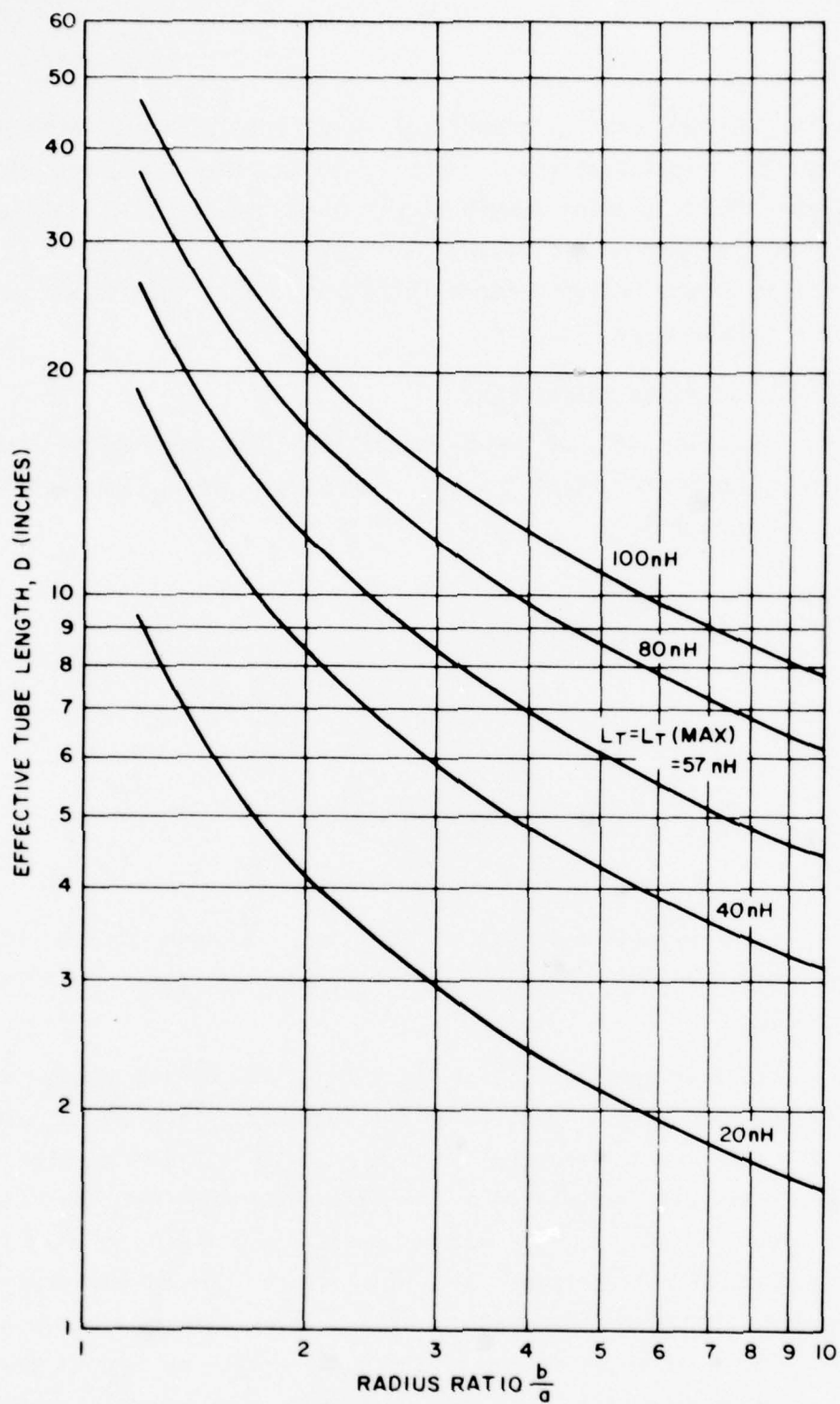
Figure 10. Maximum permissible tube length to be consistent with various total inductances as a function of the radius ratio b/a. The value L_T = 57 nH is consistent with a 40 kA current pulse having a rise time of 20 nS.

We know that a cathode area of at least 500 cm^2 will be required for a 40 kA, 60 nS pulse. This implies at least a 4.5-inch O.D. tube, which, after the addition of flanges and guard rings, will have an effective diameter for stress purposes of about 6 inches (a = 3).

We know that we must not operate too far removed from optimum stress conditions, and that stress will be minimized at maximum b. Setting $b/a = \epsilon$ with $b = b_{max} = 7$, we find a = 2.6.

We are now in a position to determine the required number of gaps on the basis of b = 7 and a grid structure that is consistent with a 500 cm^2 cathode. To do this, we first determine the stage-to-stage capacitance, C_1, for a typical 4.5-inch tube. Then we establish the stage-to-ground capacitance, C_2. Finally we investigate the voltage division across the gaps as a function of the number of gaps at the appropriate ratio of C_1 to C_2. For typical gap spacings of 0.125 inch (E-E) and center-to-center spacings of somewhat less than an inch, the stage-to-stage capacitance is both calculated and measured to be of the order of 35 to 40 pF. From Equation 8, assuming a = 2 inches for a 4.5-inch tube and with b = 7, we calculate C_2 to be 0.94 to 2.8 pF depending on ϵ_r. Thus the range for the ratio C_1/C_2 is 12.5 to 42.6, or roughly 10 to 40.

Figure 11 shows the result of a calculation to determine the voltage across the top segment as a function of the total number of segments, N, for various values of the ratio C_1/C_2. In an ideal case ($C_2 = 0$, C_1/C_2 infinite), the voltage across the top segment would vary as 1/N. As Figure 11 clearly shows, the effect of low C_1/C_2 is to cause the top segment voltage to become independent of N and also to be established at a high level.

Consider a case with N = 10. Ideally, the voltage across the top segment would be one-tenth of the applied voltage. From Figure 11, at N = 10 with $C_1/C_2 = 20$ (the geometric mean over the range of interest), the voltage across the top segment is over 20% of the applied voltage, i.e., the stress has been enhanced by over 100 percent. Figure 12 shows the effect just described for the full range of N. In the ideal case, the enhancement would be zero for all values of N.
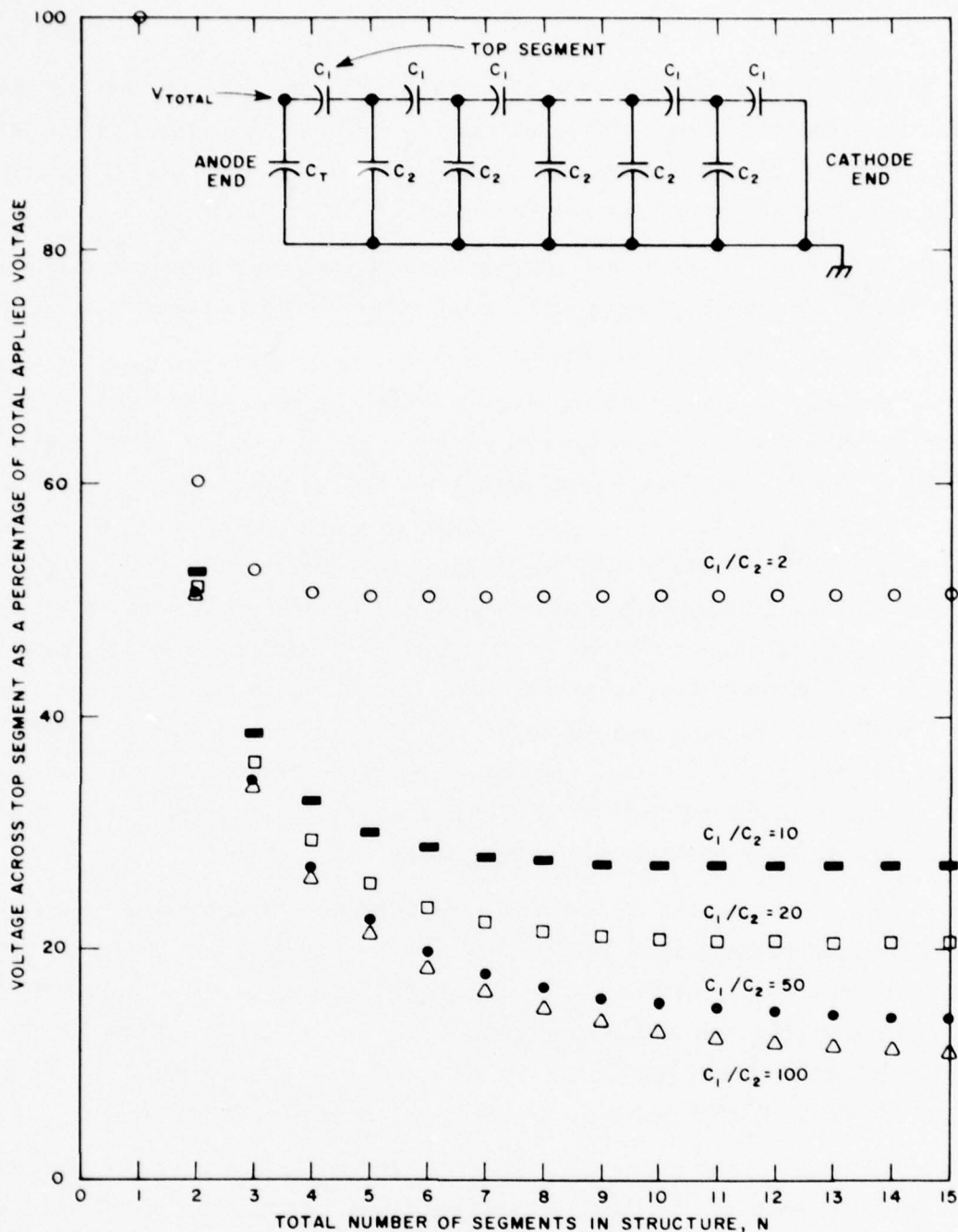
Figure 11. Voltage across top segment of a multisegment structure expressed as a percentage of the total voltage applied to the structure and shown as a function of the total number of segments comprising the structure. Capacitive transient distribution is assumed, and curves are shown for various values of the ratio C_1/C_2. In the ideal case ($C_2 = 0$), the voltage would be distributed uniformly across the segments, with each segment bearing $1/N$ of the applied voltage.

-32-
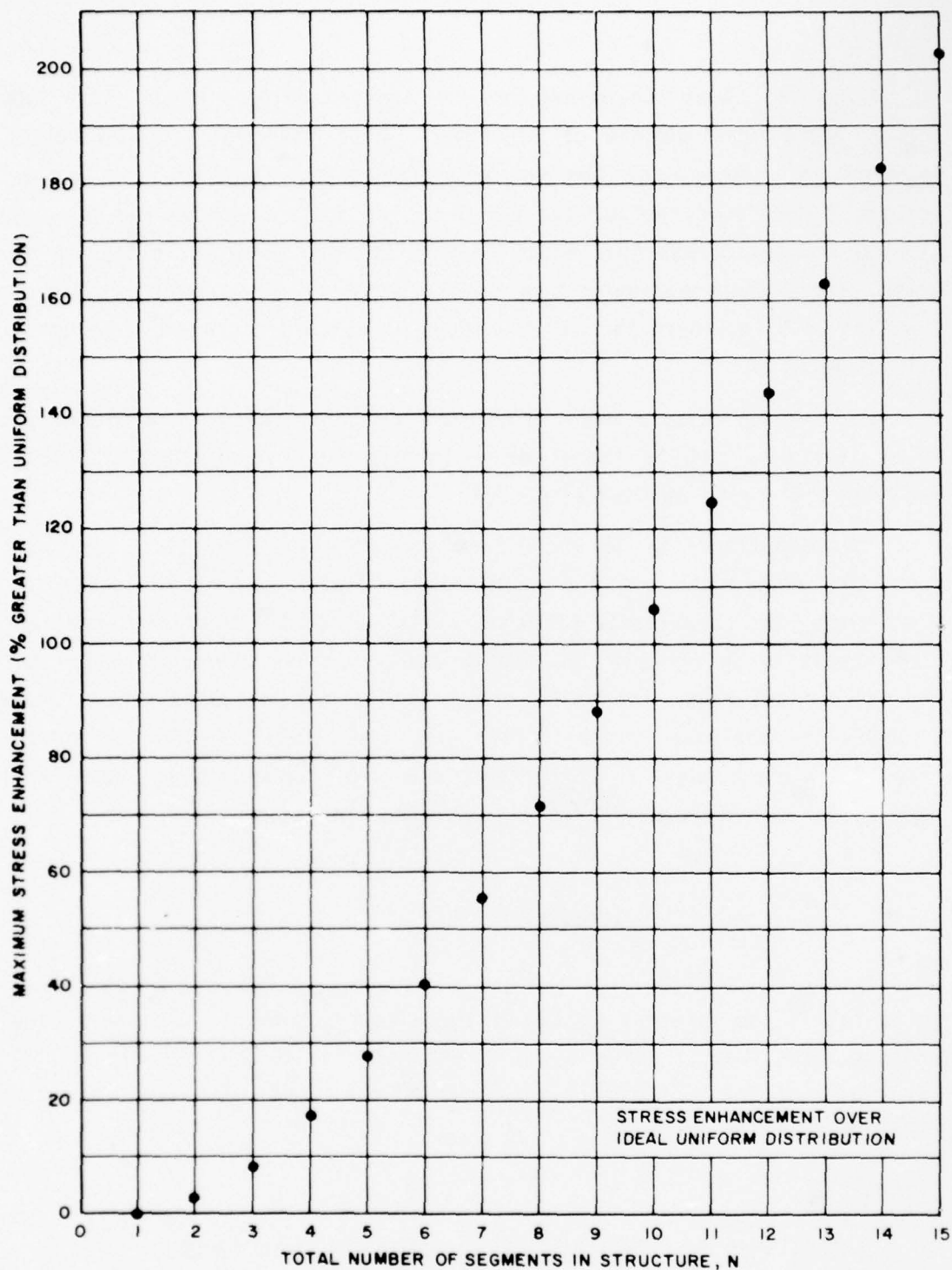
Figure 12. Maximum stress enhancement over the zero value that corresponds to the ideal uniform voltage distribution. The curve corresponds to $C_1/C_2 = 20$. For higher C_1/C_2, the curve tends to zero, and for lower C_1/C_2, the curve steepens.

Figure 13 shows the percent of the applied voltage across each segment for various total numbers of segments. Note that for a given number of segments, N, the sum of the voltages across all segments must equal 100 percent. More importantly, the ratio of the voltage across the top segment (i = N) to that across the bottom segment (i = 1) serves as a measure of the gross stress distribution across the structure. This ratio is shown as a function of N in Figure 14. In the ideal case, this ratio would be unity for all values of N.

It is clear that a high value for the ratio C_1/C_2 is a highly desirable situation. It is therefore worthwhile to investigate the parametric dependence of C_1/C_2 at some length.

The capacitance C_1 is the interelectrode capacitance of each gap. As such, its components are the capacitance between the active areas of the electrodes, the capacitance present by virtue of the dielectric constant of the interstage spacer and the appropriate effective area, and such further capacitance as arises due to the external flanges and guard rings. We will simplify the analysis by considering only the capacitance due to the active area of the electrodes, realizing that the other components are nontrivial but work to our advantage by increasing C_1. Thus we assume

$$C_1 = \pi\varepsilon_0 \, a^2/d \quad \text{farads per stage} \tag{21}$$

where "a" is the internal radius of the electrodes and "d" is the interelectrode spacing (E-E). If we assume for simplicity that the dimension "a" may also be used for a rough calculation of the stage-to-ground capacitance, then

$$C_2 = \frac{2\pi\varepsilon_0\varepsilon_r}{\ln b/a} \quad \text{farads per stage per unit stage length} \tag{22}$$

-34-
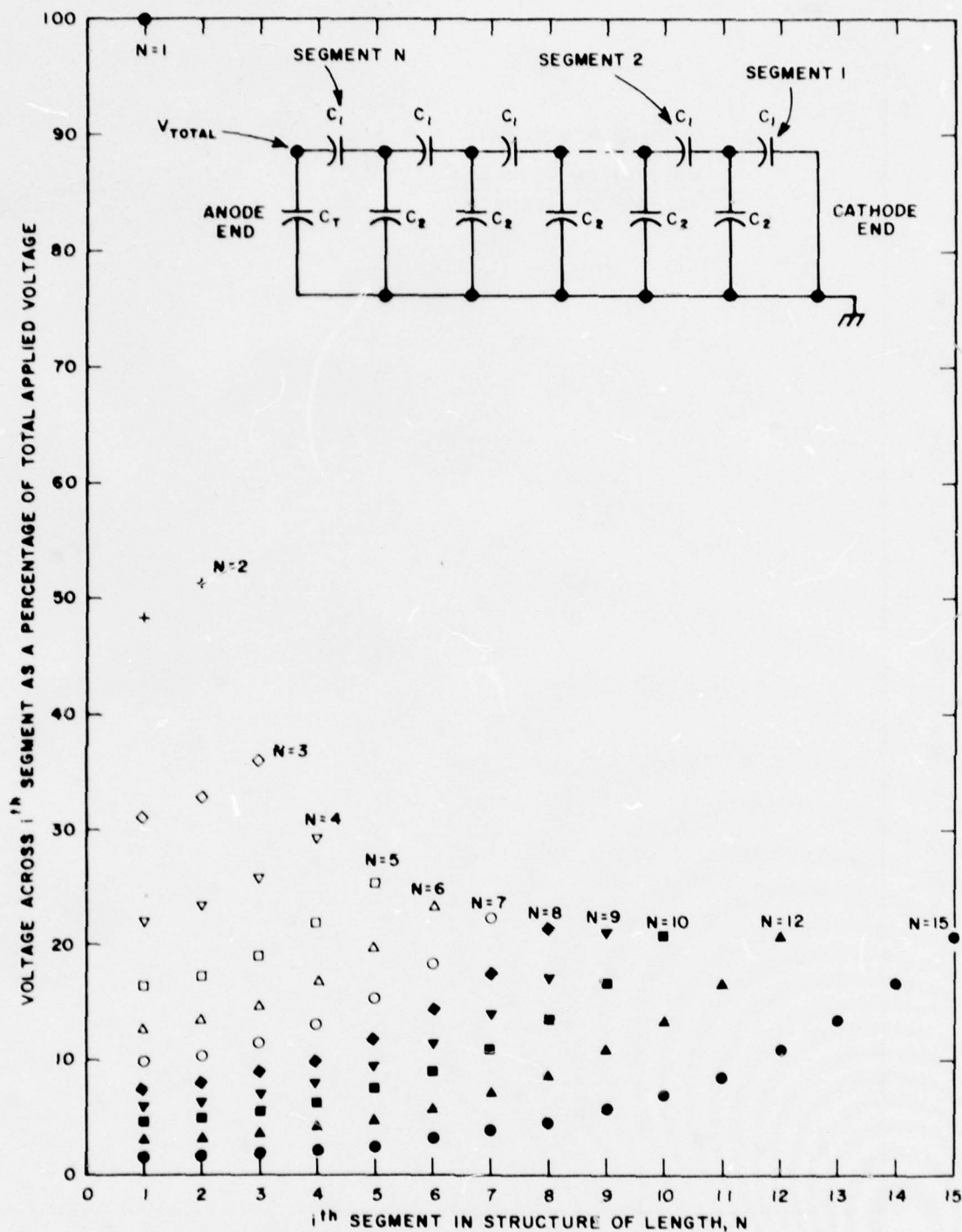
Figure 13. Capacitively distributed voltage across each segment of a multi-segment structure for structures comprised of various numbers of segments. The curves assume a capacitance ratio, C_1/C_2, equal to 20. The voltage is always higher across the top segments.

-35-
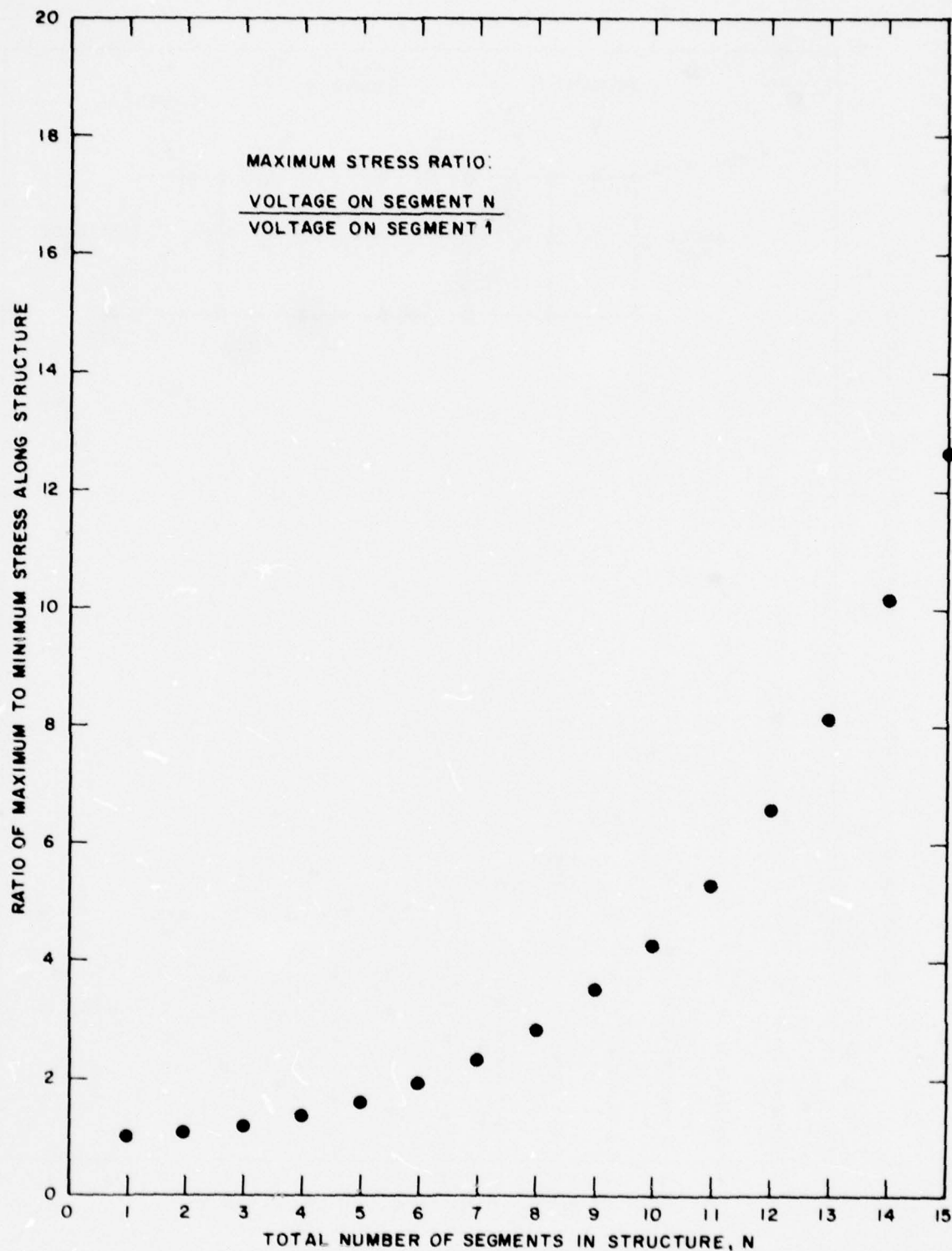
Figure 14. Ratio of the maximum to minimum stresses across the various segments of multisegment structures. A value of $C_1/C_2 = 20$ is assumed. The lower the stress ratio, the more uniform the gross distribution across the structure.

-36-

Thus

$$\frac{C_1}{C_2} = \frac{a^2}{2\varepsilon_r d} \ln \frac{b}{a} \quad \text{per unit stage length} \tag{23}$$

Equation 23 is maximized with regard to "a" and "b" when the function $a^2 \ln \frac{b}{a}$ is maximized. It is easily found that this condition occurs when

$$\frac{b}{a} = \sqrt{\varepsilon} \tag{24}$$

Substituting Equation 24 into Equation 23 we find

$$\frac{C_1}{C_2} (\text{max}) = \frac{b^2}{4\varepsilon \, \varepsilon_r d} \quad \text{per unit stage length} \tag{25}$$

which is the desired functional dependence for maximizing C_1/C_2.

From Equation 25 we observe a dependence of C_1/C_2 (max) on b^2. This is yet another argument for designing for maximum b. It is of course also clear that reducing the electrode spacing and the total stage length will increase C_1/C_2.

The relative permittivity offers little hope for relief. Gas is not a good medium for cooling the tube, although it might be feasible for burst-mode operation. With $\varepsilon_r = 80$, water is ruled out. This leaves oil, and most insulating oils have a dielectric constant of two to three.

Figure 15 shows a plot of the function $a^2 \ln \frac{b}{a}$ for b = 6 and 7 inches. It is important to note that C_1/C_2 decreases markedly for b/a less than the optimum value of $\sqrt{\varepsilon}$.
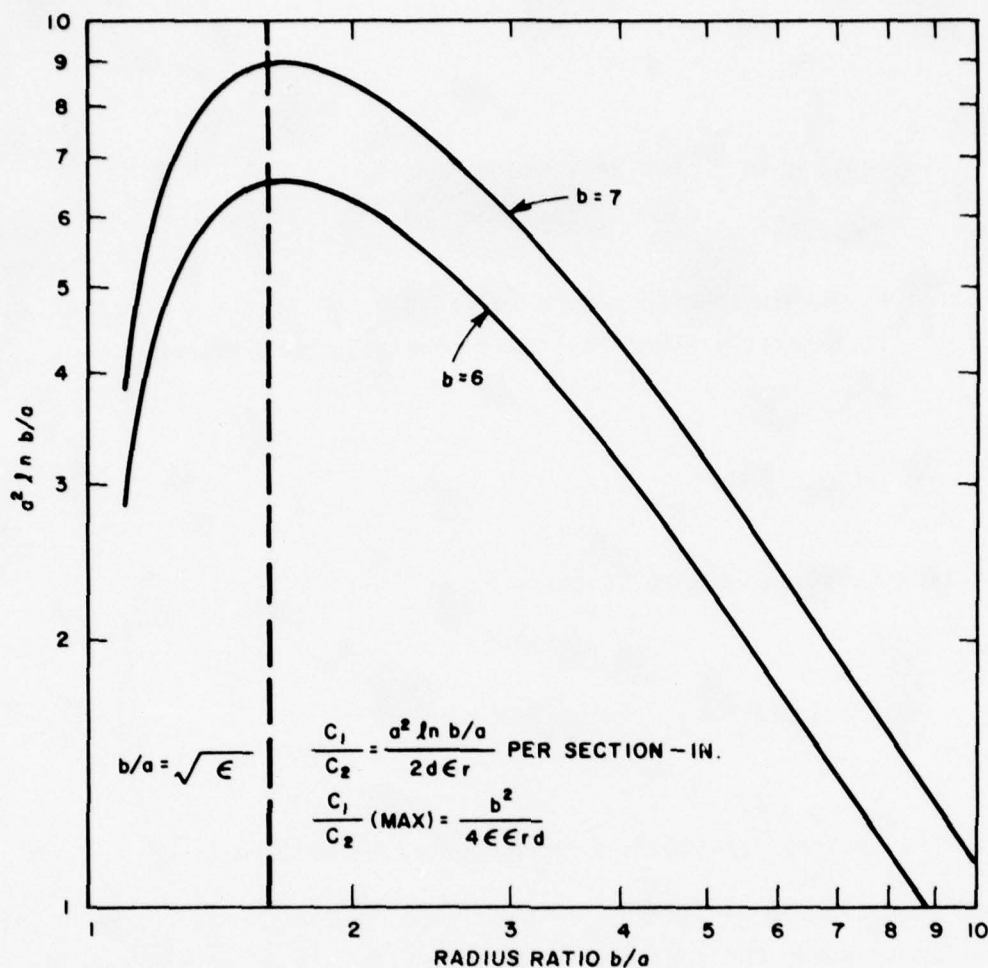
Figure 15. Plot of the function $a^2 \ln(b/a)$ as a function of the ratio b/a. The function peaks at $b/a = \sqrt{\epsilon} = 1.65$, and is proportional to b^2. The conclusions are that the ratio C_1/C_2 is optimized at b/a, and also that large b is desirable.

It is clear that the optimum number of stages, N_0, is a function of C_1/C_2. If we define N_0 as being that number of stages such that the addition of another stage will reduce the stress on the upper stage by only 10%, we can then establish N_0 as a function of C_1/C_2.

-38-

The results of such a calculation for the range of C_1/C_2 of interest are shown in Figure 16. From Figure 16, one can readily determine values for N_0 of 4, 5, and 6 for $C_1/C_2 = 10$, 20, and 40, respectively.
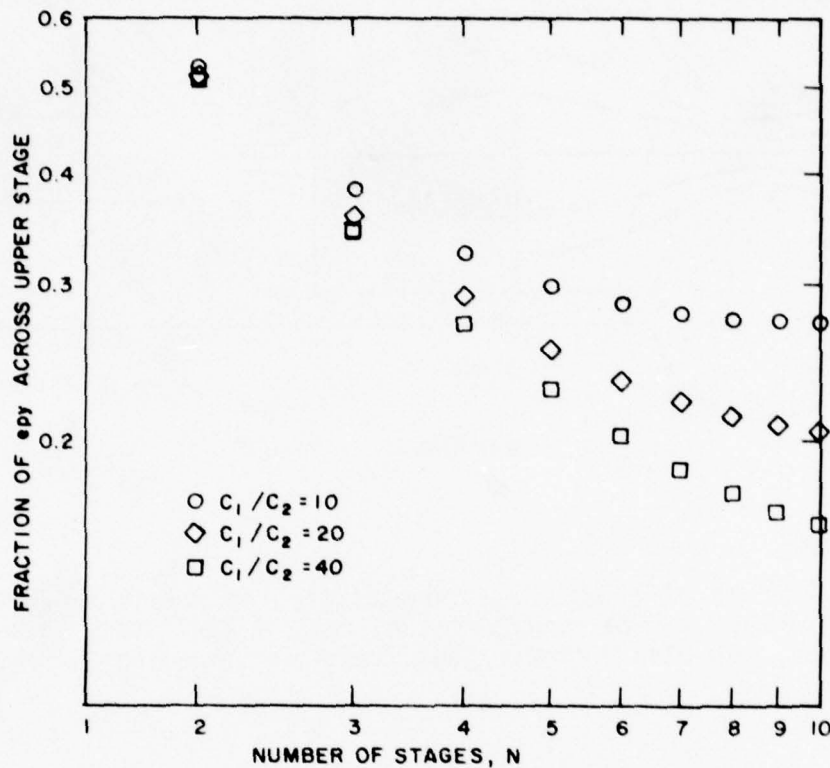
Figure 16. Fraction of epy appearing across the upper stage of multistage structures for various values of the ratio C_1/C_2. From the curves, one can determine a point of diminishing return as regards the optimum number of sections.

d.   Stress Equalization in the Grid Insulators

The scheme of Figure 17 is useful to equalize the stress at the external surface of the ceramic grid spacers. Although effective as equalizers, the guard rings increase the stray capacitance C_2 and also increase the stress in the insulating medium external to the tube.

-39-
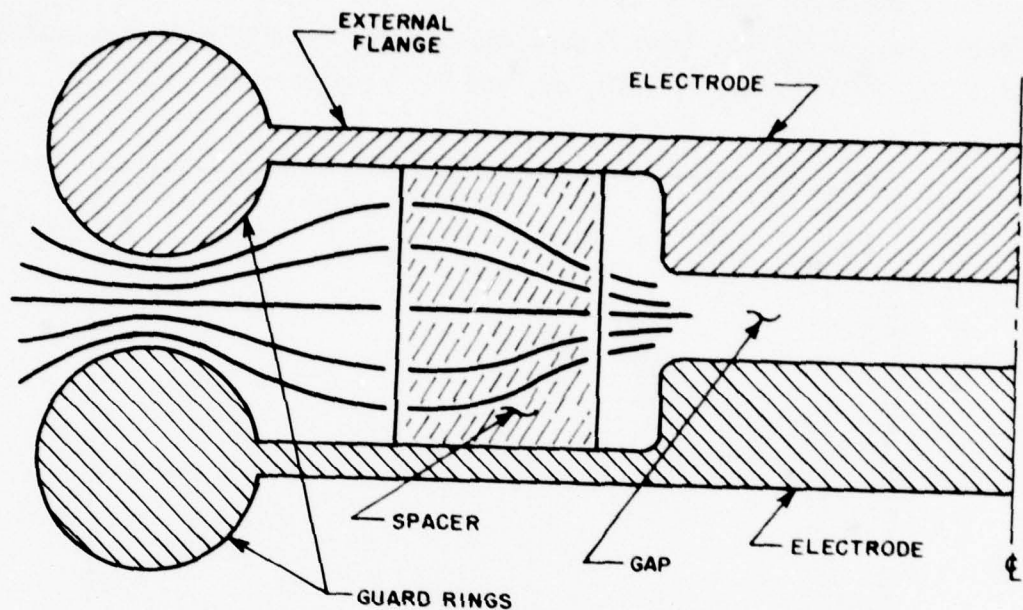
Figure 17. The use of guard rings to equalize the stress in an interelec-
trode insulator. The rings serve to control the stress pattern in the
insulator, but also increase the stress in the medium external to the
device.

The maximum stress between equal parallel cylinders (a fair approximation
for the rings) is given by (4)

$$Em = \frac{0.45 \, V_o}{r \ln \frac{D}{2r}} \tag{26}$$

where r is the cylinder radius and D is the center-to-center cylinder spacing.
(Typical values for D for a low inductance grid structure are 0.75 to 1
inch.)

-40-
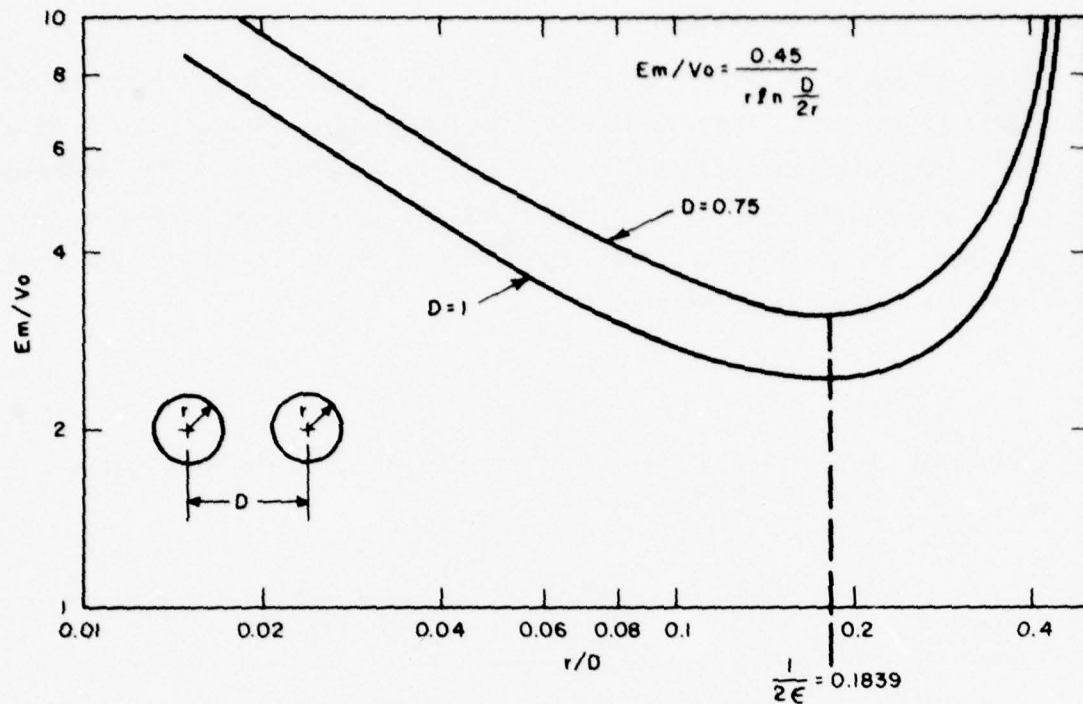
Figure 18. Curves showing the normalized stress produced by guard rings of the type shown in Figure 17. There is an optimum guard ring radius for a given ring spacing.

It is readily determined that Em is minimized when

$$\frac{r}{D} = \frac{1}{2\epsilon} \tag{27}$$

Substituting Equation (27) into Equation (26) yields

$$Em \text{ (optimum)} = 0.9 \epsilon \frac{V_0}{D} \tag{28}$$

Figure 18 shows the normalized stress, Em/V_0, as a function of the ratio r/D for $D = 0.75$ and 1 inch. The dependence on D and the minimum at $r/D = \frac{1}{2\epsilon}$ are observed.

-41-

e. Interaction of Parameters

The design of a practical high voltage, low inductance tube is not a straightforward task. The various design parameters interact in a complex fashion, and an optimum design is not readily apparent. It is, therefore, helpful to tabulate the various interactions so that an overview can be established. To do this, we first define our terms as in Table 3 and then we consider the concepts of Table 4.

Table 3. Definition of terms used in the design of a high voltage, low inductance tube.

Term	Definition
epy	Holdoff capability of tube
tr	Rise time of tube current
τ_i	Ionization time constant of tube
P	Gas pressure in tube
N	Number of stages
E-E	Electrode spacing
e_r	Permittivity of insulating medium about tube
2b	Inner diameter of coaxial current return
2a	Effective diameter of tube
C_1	Interelectrode capacitance
C_2	Stage-to-ground capacitance
Ec	Maximum stress in ceramic (stage-to-stage)
Ei	Maximum stress in insulating medium
L_T	Tube inductance
DGBV	Dynamic gas breakdown voltage (per stage)

Table 4. Summary of design compromises.

Variable	Chain of Principal Effects	Fundamental Compromise	Determining Factor, or Fundamental Limits	Practical Considerations	Good Effects	Bad Effects	Comments
P	Affects τ_i; thus τ_r; also exposure time for E_c and E_i	τ_r vs epy	Must avoid DGBV		High P reduces τ_r, also reduces exposure time for E_c and E_i	High P reduces epy	Must determine a compromise (involving charging time) experimentally
N	Affects epy and L_T directly, E_c and E_i indirectly	L_T vs epy	C_1/C_2; DGBV	Many sections means many seals	Large N implies good epy (if C_1/C_2 is high)	Large N implies long tube, therefore high L_T	
E-E	Affects C_1; thus C_1/C_2; thus N; thus epy; also L_T and E_c	L_T vs epy	Must avoid field emission breakdown and DGBV	Mechanical constraints apply for small E-E	Small E-E increases C_1/C_2 - is consistent with short grids if E_c allows		Relatively minor degree of freedom
ε_r	Affects C_2; thus C_1/C_2; thus N; thus epy; also L_T and E_c	C_1/C_2 vs epy; therefore L_T vs epy	Property of insulating medium	Options are limited		High ε_r decreases C_1/C_2	Will probably use oil $(\varepsilon_r=2-3)$ for good cooling and avoidance of pressurized gas
2b	Affects L_T and C_2; thus C_1/C_2	L_T vs epy	Available space; required C_2	Available space	Large "b" good in general - aids L_T, C_1/C_2, E_i		Design for maximum "b" (7-10 inches)
2a	Affects L_T; also C_2; thus C_1/C_2; thus N; thus epy	L_T vs epy	Cathode size and L_T for small "a"; low C_1/C_2 and high E_i for large "a"	"a" for stress and C_2 considerations always larger than "a" for inductance purposes; a=6 is upper practical limit for ceramic seals	Large "a" reduces L_T, is consistent with large cathode	Large "a" reduces C_1/C_2	Want maximum "a" consistent with good C_1/C_2 and acceptable E_i

-43-

It is clear from Table 4 that there are too many dependencies acting at cross purposes to allow a straightforward determination of the optimum design. It is thus desirable to bound the problem by making some simplifying (but justifiable) assumptions. It is also required to perform experimental work in some areas to determine the extent to which practical considerations limit design freedom.

f.   Simplifying Assumptions

(1)   Relative Permittivity, e_r

We shall assume that the insulating medium between the tube and its environs will be oil (as opposed to gas) in spite of the significantly higher relative permittivity of oil. We choose oil because it is highly effective as a coolant for the tube, and more importantly, has a relatively sluggish breakdown characteristic. Since all of the voltage stresses resulting during the operation of a high voltage, low inductance tube are of a transient nature, the slow breakdown of oil can be used to advantage by designing the system to operate at higher stress levels than those that are permissible with gas. (Because of its dielectric constant of 80, water cannot be used as the insulating medium.) We presently feel that gas should be considered as the insulating medium only if the ultimate requirement for C_1/C_2 is such that the required values for epy and L_T cannot otherwise be achieved.

(2)   Diameter of Current Return, 2b

We elect to design for the maximum available space, i.e., a return diameter of 14 to 20 inches. We do so for various reasons. First, from Equation (25), operation at maximum b will optimize C_1/C_2 (hence N and thus epy) for any value of e_r and E-E spacing. Second, operation at maximum b will reduce the stress, E_i, for any given b/a. Finally, operation at maximum b for a given value of b/a will provide the maximum space for a short, substantially planar cathode.

-44-

g. Triggerability vs Holdoff

We assume that holdoff and recovery (as opposed to triggerability) will ultimately dominate tube performance. This assumption is based largely on our experience with hydrogen thyratrons, and is not otherwise readily apparent. Theoretical work is presently underway to definitize the tradeoffs that exist as regards triggerability versus holdoff as a function of aperture width, aperture offset, and E-E spacing.

The depth of our confidence that triggerability can be assumed is tacitly implied by our design for an experimental tube as described later in this document.

h. Necessary Experimental Data

The degree to which the ceramic insulators can be stressed is not known, nor can it be established without experimental work. A typical manufacturer's data sheet indicates a stress capability of 225 volts/mil for a quarter-inch sample at room temperature. Obviously this does not mean that a one-inch piece would withstand 225 kV, particularly at elevated temperatures, and particularly under repetitive, fast pulse conditions. It is necessary for us to have design information of this nature if we are to build a successful high voltage, low inductance tube. This need caused us to enter into the ceramic evaluation study described below.

(1) Ceramic Evaluation

(a) Samples

The ceramic insulators between the various electrodes of the tube must be physically short to establish the tube's inductance, L_T, at its required value. As a result, they are subjected to severe voltage stress during both the charging and commutation periods. During the charging cycle (for perhaps 10 microseconds), the voltage, epy, divides across the various gaps as described in Section 4c. Depending on the ratio C_1/C_2 (which effectively limits N), the voltage across the upper stages can be materially

-45-

greater than 1/N. Furthermore, as the tube cascades (some tens of nano-seconds), an ever-larger fraction of epy appears across the unfired gaps until finally the full voltage, epy, appears across the last unfired gap and its corresponding insulator. For the voltages and insulator lengths applicable to this Program, the resultant insulator stress is well above that encountered in standard practice.

To determine the stress capabilities (under pulsed conditions) of suitable ceramic insulators, we procured samples of various ceramics and built a 250 kV Marx generator to serve as a pulsed high voltage source for testing the samples. A typical sample (fitted with suitable electrodes) is shown in Figure 19. The electrodes were designed to provide a uniform stress pattern in the sample, and also to provide a convenient means for lead attachment. Each sample was metalized over the area corresponding to the center third of its diameter, and the electrode subassembly was then brazed to the metalized area.

All samples are three inches in diameter and 0.25-inch thick. The thickness was chosen to be thin enough so that a rupture at high voltage is likely. This ensures the occurrence of a definitive event under measurable conditions. On the other hand, the pieces are thick enough so that the results can be scaled to appropriate thicknesses.

The breakdown characteristics of ceramics depend on their thermal history. It was thus necessary to monitor the time-temperature cycle neces-sary to achieve a high-quality and essentially simultaneous brazing of the two electrodes to the metalized ceramic.

About one-half of the samples were metalized by the vendor, with the remainder being metalized by EG&G using the hydride process that we employ for much of our tube fabrication. All assemblies were brazed in a vacuum furnace, and have thus been cycled exactly as they would be if they were being used in the construction of an actual tube.

Table 5 shows the various combinations of circumstances that corre-spond to the entire lot of samples. The total number of pieces is fifty-five.
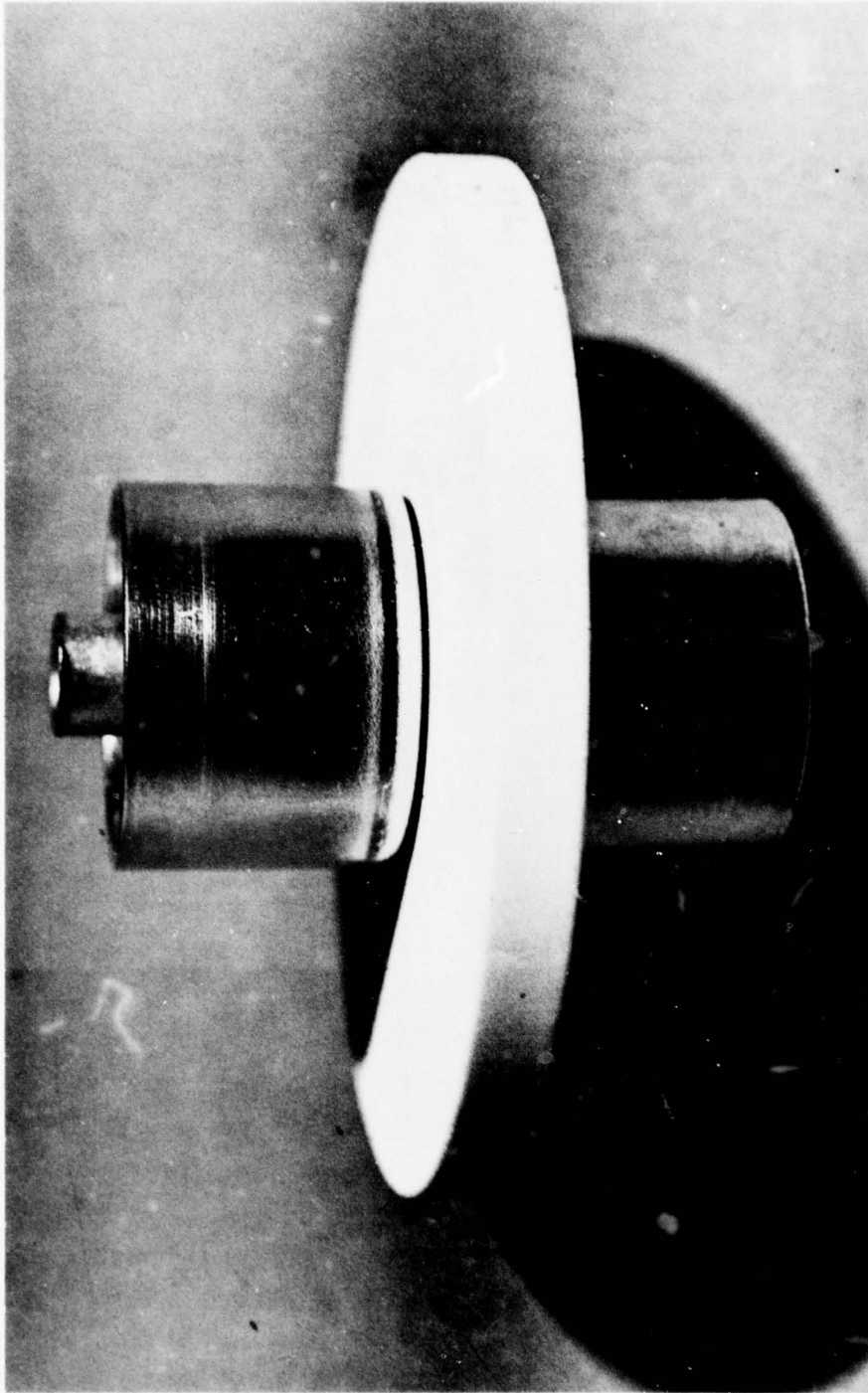
Figure 19. Ceramic test sample with electrodes. The ceramic is three inches in diameter and 0.25-inch thick. The sample is thin enough to yield definitive results, and thick enough so that the results can be scaled to suitable thicknesses.

Table 5. Ceramic samples for evaluation study.

Vendor and Material	Sample Size	Metalization
Alberox--A-950	20	Alberox
Alberox--A-950	10	EG&G
Wesgo--AL-300	10	Alberox
Wesgo--AL-300	5	EG&G
Diamonite--Chrome Oxide Doped*	10	EG&G

*These pieces were rendered slightly conductive by the addition (in bulk) of a conductive material. Conductive ceramics might be useful to provide resistive grading along the lengths of the insulators. All ceramics have some leakage, and the leakage current at the given voltage increases with temperature. Therefore, even the undoped ceramics will provide a minor degree of resistive grading.

(b) Marx Generator

A photograph of the 250 kV Marx generator is shown as Figure 20. The device was characterized and the results of this effort are shown in Table 6. Note from Table 6 that the equivalent circuit for the erected Marx is 0.01 μF in parallel with 10 K ohms, with that combination being in series with 1.5 μH. This equivalent circuit is important in two respects. First, the 100 μS decay characteristic of the device is consistent with the time-stress profile the ceramics must endure during the 10 μS charging cycle. (The decay time can be reduced by preloading the generator.) Second, the 1.5 μH inductance (resulting principally from the output lead geometry consistent with 250 kV of insulation in air) is sufficiently high to cause resonant charging of the sample's capacitance (10 pF) with a period of sufficient length to perturb the results of the testing. We have investigated this effect by using the Marx generator to determine the dynamic breakdown voltage
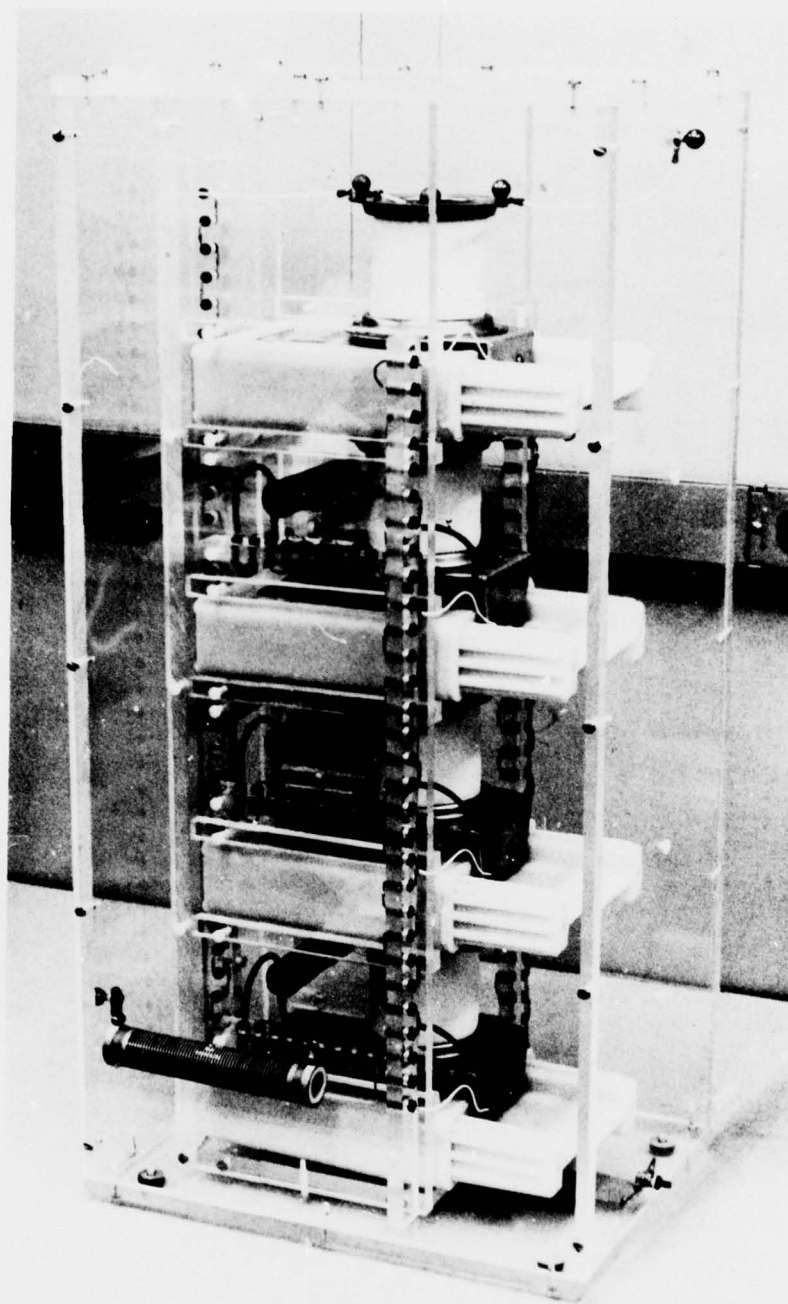
Figure 20. Marx generator for testing the ceramic samples. The device produces 250 kV. When erect, its equivalent circuit is 0.01 µF in parallel with 10 K ohms, with that combination in series with 1.5 µH.

-49-

of a vacuum spark gap, and resonant charging effects were indeed observed. To preclude resonant charging (which doubles the voltage applied to the sample under test), it is necessary to add resistance in series with the generator. This limits the rise time of the voltage waveform at the load, but permits the establishment of a controlled time-stress profile.

Table 6. Characteristics of Marx generator for ceramic sample evaluation.

Number of stages	4
Capacitance per stage	0.04 μF
Equivalent capacitance when erect	0.01 μF
Charging time	16 sec
Maximum input voltage	65 kV
Maximum output voltage	260 kV
Maximum working output voltage (Note 1)	240 kV
Energy stored at 60 kV input	288 Joules
Total time to erect (Note 2)	800 nS
Output voltage rise time	100 nS
Short circuit current (Note 3)	14 kA
Equivalent shunt resistance	10 K Ohms
Equivalent series inductance (Note 4)	1.5 μH

Notes:

1. For input voltages greater than 60 kV, the spark gaps occasionally flash over externally. This limits the output voltage to 240 kV for trouble-free operation.

2. Total of gap delays and output voltage rise time at 240 kV (open circuit).

3. Measured when discharging the device into a nine-inch arc with 55 kV input.

4. Calculated from measurements of the ringing frequency under the conditions of Note 3.

(c) <u>Other Testing</u>

At the time of this writing, the quantity of ceramic-electrode assemblies thus far produced does not warrant the initiation of the ceramic evaluation tests. If the ceramics perform well, an important degree of design freedom will be established. If they do not, we will at least have the required information concerning the limits of their stress capabilities. Even if the ceramics perform well at high stress, the effects of two important variables — temperature and pulse repetition rate — will remain to be investigated. We thus plan to subject samples to high voltage pulses at high pulse repetition rates using various test kits at our facility. The ultimate test is, of course, the operation of an actual experimental tube.

5.0 FIELD PLOTS AND MATHEMATICAL MODEL FOR THE TUBE

It is clearly desirable to perform parametric studies on paper whenever possible, thus reserving expensive laboratory experimentation for those areas where paper studies are ineffective (e.g., ceramic evaluation), or to verify some theoretically predicted result. Two areas where theoretical work has been particularly helpful to this program are field plotting and mathematical modeling of the tube's anode fall characteristics. Both of these are discussed briefly below.

a. Field Plots

Computer-generated field plots are of great value in the design of insulator and electrode shapes that minimize voltage stress. A typical example is given by Figures 21 and 22 which show the field patterns that result from differing designs for the interstage insulators. The information gained from the particular plots shown is that the field is concentrated in the vicinity of the ceramic-to-metal seals, and that the recessed type of insulator (Figure 22) provides the better overall stress situation.

The differences in stress patterns to be expected for a 5-segment tube structure under uniform and capacitively determined voltage distributions is illustrated by the plots shown in Figures 23 and 24, respectively. The plots correspond to a 5-inch tube operated with a 12-inch current return. The relative permittivity of the insulating medium is assumed to be unity. For the capacitance-controlled case under consideration, 25.4 percent of the applied voltage appears across the upper gap. The plots show the extent to which the fields are intensified in the upper ceramic insulators and in the external insulation nearby.

b. Mathematical Model

We have developed a mathematical model for the hydrogen thyratron that predicts with reasonable accuracy the overall shape of the anode circuit current pulse (including its early exponential rise), the peak current and the time of the peak current, the pulse width, and the apparent increase in anode fall time that is observed in practice for tubes operated at high di/dt. The impetus for developing such a model was to perform on paper parametric studies that would be cost and time prohibitive if performed in the laboratory.
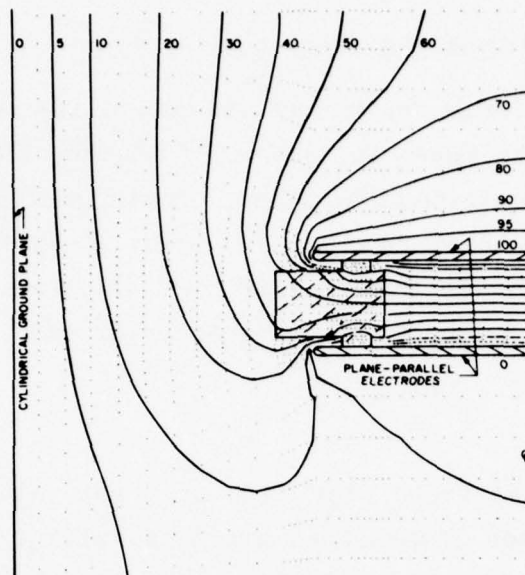
-53-

Figure 21. Representative computer-generated field plot. This plot shows the stress pattern in an interelectrode spacer having projections beyond the electrode flanges, and should be compared with the plot of Figure 22.
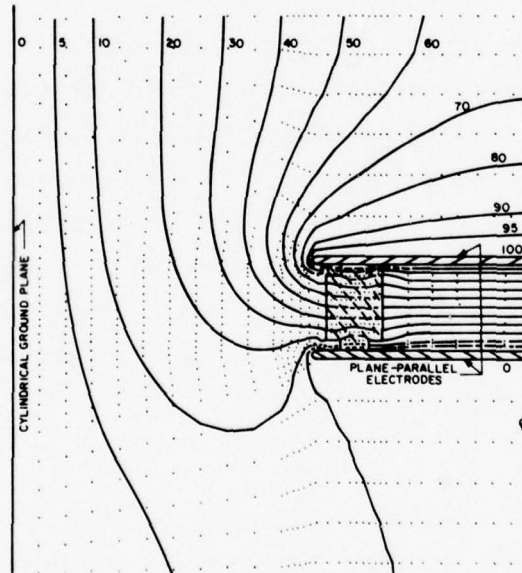

Figure 22. Field plot showing the stress pattern in an interelectrode spacer that is recessed with respect to the electrode flanges. The plot should be compared with that of Figure 21. The conclusion is that the field is equally concentrated at the seals for both spacer designs.
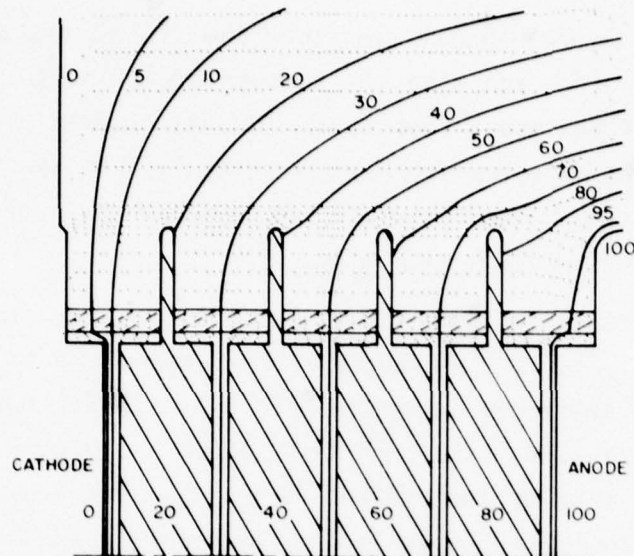
Figure 23. Field plot corresponding to a five-section tube under uniform voltage distribution. This plot should be compared with that of Figure 24.
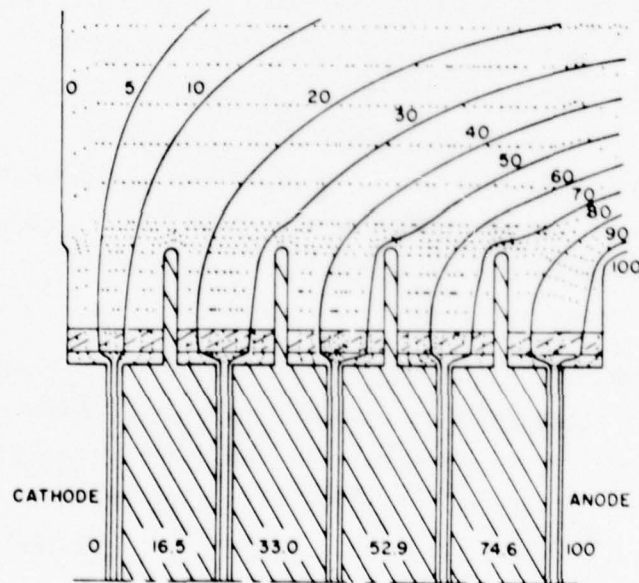

Figure 24. Field plot for a five-section tube under capacitively controlled voltage distribution. This plot should be compared with that of Figure 23 to reveal the enhanced upper-section stresses that apply in the capacitance-controlled case.

The Appendix to this report describes the assumptions and technique used to establish the model and also the circuit equations that result from its use. The value of the model lies in its ability to predict trends in circuit behavior that would be quite difficult to establish without extensive experimental investigation. The curves of Figure 5 of this report are a typical example, and another is discussed below.

The oscillogram of Figure 25a shows the anode current, i(t), and the anode voltage, eb, of a hydrogen thyratron operating in a low inductance circuit where the thyratron's inductance and the inductance of the remainder of the circuit are comparable such that di/dt is high. Observe first the early exponential rise of the current as the tube ionizes. Observe also the relatively long anode fall time (65 nS full-fall) and also that the anode voltage does not reach zero until the peak of the current pulse (where di/dt is zero). Note finally that the anode swings negative in a more or less sinusoidal fashion.

Refer now to the oscillogram of Figure 25b which shows the performance of the same tube when operated at the same hydrogen pressure but with a circuit inductance that is roughly 25 times that corresponding to Figure 25a. We term this a condition of low di/dt. Note that the sweep speed in Figure 25B is 20 nS/minor division as opposed to 10 nS/minor division so that the peak of the relatively slow current pulse can be observed. The current sensitivity has also been increased in Figure 25b to permit a full scale deflection at the lower currents corresponding to the higher inductance.

In Figure 25b, the obvious effects of increased circuit inductance are to widen the current pulse and decrease its amplitude. The more subtle (and more interesting) effect is to decrease the anode fall time (full-fall) to something of the order of 10 nS. Observe also that the anode voltage no longer swings negative. Instead, it slopes off gently to the value corresponding to the steady-state tube drop.

The overall conclusion from Figure 25 is that the voltage drop across the tube's inductance (L_T di/dt) is dominating the apparent anode fall time in Figure 25a. This theory fits all observations exactly. Note, for example, in

(a)

(b)
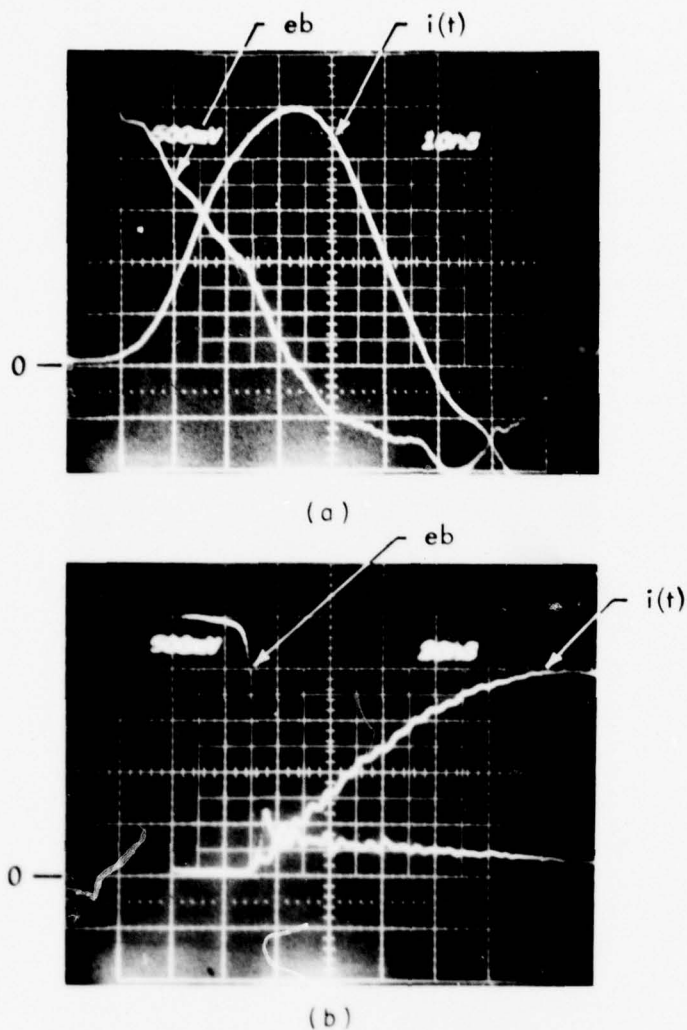
PRESSURE = 400 MILLITORR.
           a) HIGH di/dt
           b) LOW di/dt
VOLTAGE: 500V/MINOR DIV.
CURRENT: a) 200A/MINOR DIV.
           b) 40A/MINOR DIV.
TIME: a) 10 NS/MINOR DIV.
        b) 20 NS/MINOR DIV.

Figure 25. Oscillograms showing the anode fall and current rise of a hydrogen thyratron under conditions of (a) high di/dt and (b) low di/dt. Note that the tube's inductance causes the anode fall to lengthen in the high di/dt case due to the voltage drop across the tube's inductance. Note also the early exponential increase in the current (high di/dt case) as the tube commutates.

Figure 25a that eb is zero when di/dt is zero. Observe also that eb is about at its negative maximum when the current crosses the zero-axis, i.e., when di/dt is at its negative maximum. Observe also from Figure 25b that when di/dt is low, inductive drops in the tube are low. Thus eb falls quickly to near-zero, and thereafter, eb slowly decreases to the steady-state tube drop as di/dt slowly decreases to zero at the peak of the current pulse.

Refer now to Figure 26, which shows the waveforms calculated for i(t) and eb using the model for both the high and low conditions of di/dt (Figures 26a and 26b, respectively). Conditions approximating those of Figure 25 were assumed. The waveforms shown in Figure 26 were normalized to their respective peaks so that the curves would have the same aspect ratio as the oscillograms of Figure 25.

It is not necessary to describe every detail of Figure 26 since a comparison of Figures 26 and 25 clearly reveals that the model accurately predicts the tube's behavior. Two differences, however, are worthy of note. The first is that the model makes no provision for the steady-state tube drop. Therefore, in Figure 26b, eb reaches ground at the peak of the current pulse. This is of no particular consequence.

A more important difference is shown by the dashed portion of the waveform for eb in the high di/dt case of Figure 26a. The model predicts the solid curve, and anode waveforms having such discontinuities have in fact been observed in practice for tubes operating at high di/dt in some applications. The dashed line is an approximation to what is actually observed in the oscillogram of Figure 25a. The conclusion is that for early times the actual tube inductance is a time- or current-dependent variable, with L_T (and hence L_T di/dt) being initially somewhat larger than its steady-state value. This notion is consistent with the concept of a finite time being required for the discharge to propagate radially within the tube, and the model makes no provision for such an effect. The significance of a time-varying tube inductance (and also resistance) is not yet clear, and the matter is subject to further theoretical and experimental study.
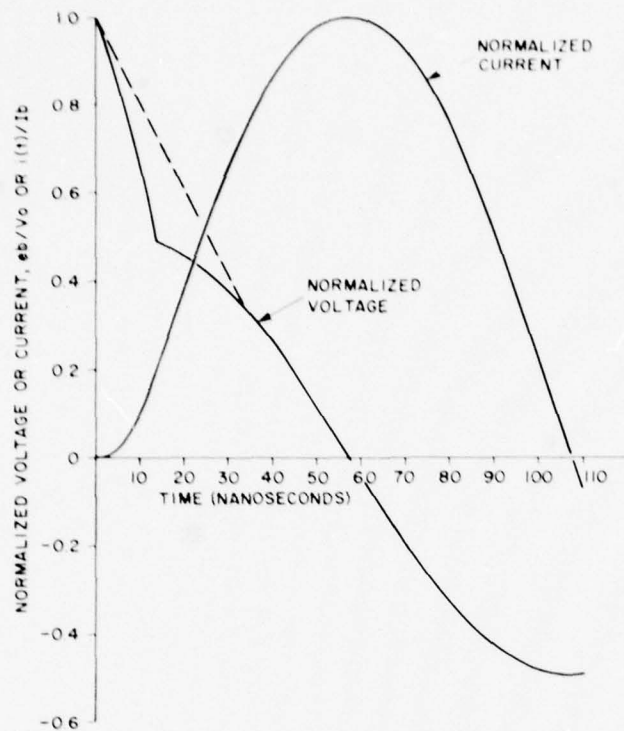
(a)
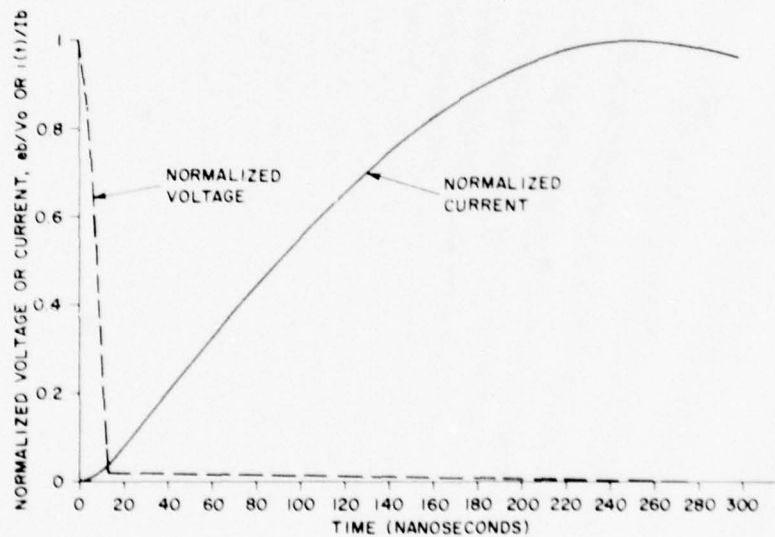
(b)

Figure 26. Current and anode fall as predicted by the model for conditions of (a) high di/dt and (b) low di/dt. The model accurately predicts tube and circuit behavior, as a comparison of Figures 26 and 25 reveals. The dashed line in the high di/dt case corresponds roughly to the actual data of Figure 25a, while the solid curve shows the waveform predicted by the model. The difference is attributed to a time-varying thyratron impedance during the commutation interval, and the model makes no provision for such an effect.

-59-

6.0 EXPERIMENTAL HIGH VOLTAGE, LOW INDUCTANCE TUBE

a. The Need for a Full-Scale Experimental Tube

Even when addressed separately, the various thyratron operating conditions pertinent to this Program are severe. It is clear that considerable research is required to achieve the ultimate objective (actual tubes that meet the operating conditions), but time and money are not without limits. It is thus necessary to develop a plan of attack that avoids the pitfalls common in design studies. The worst such pitfall is to study the wrong problem. This prompted us to design and build the first experimental high voltage, low inductance tube. We have designated this device as the HY-5505. Its purpose is to serve as a vehicle to determine where the problems really lie when one attempts to operate a multigap tube at high voltage and high di/dt. No amount of paper studies or scaled-down experiments can provide this information as quickly and as cost effectively as can a full-scale experimental device.

b. Design Philosophy

The HY-5505 is shown in cross-section in Figure 27. Its basic design is representative of our current thinking on how a high voltage, low inductance hydrogen thyratron should be built. Nevertheless, we have not departed so far from established design principles that the design could be considered radical. We expect the tube basically to work, i.e., be triggerable, have reasonably good holdoff and recovery capabilities, and operate with reasonable tj, tad, and di/dt. If such is not the case, we will have learned early where our research efforts had best be concentrated. It may, for example, be necessary to do considerable experimental work with various grid aperture configurations to establish an optimum compromise between holdoff and triggerability. It may be that the upper insulator design has no hope of working at the stress levels we expect to impose, in which case a dramatically different design will have to be developed and investigated experimentally.

It is not prohibitively expensive for us to build scaled-down tubes to investigate such aspects of the overall situation as may be required, and undoubtedly we will need to do so. It is nonetheless possible that the

-61-

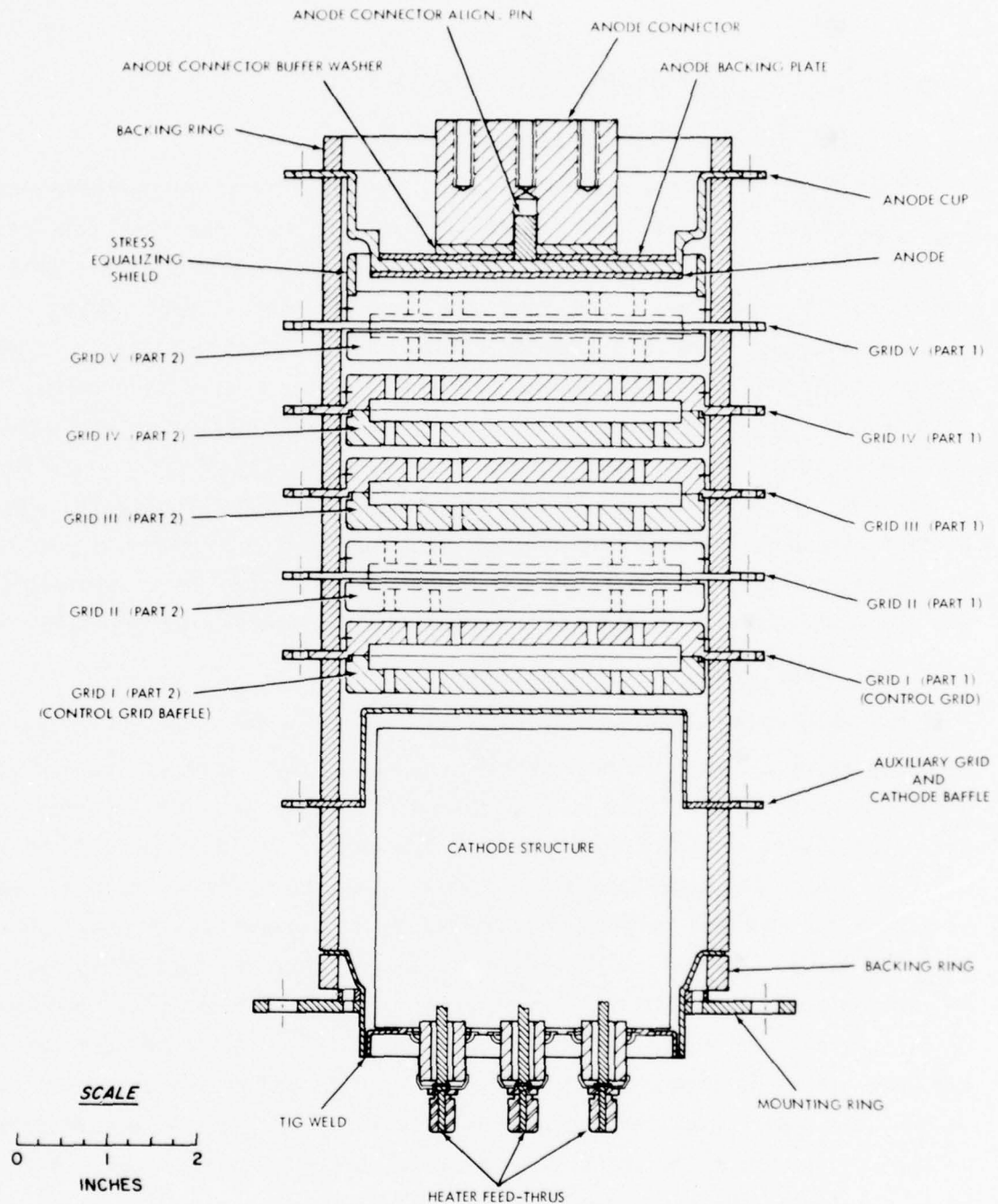Figure 27. Cross-sectional drawing showing the essential features of the first experimental high voltage, low inductance hydrogen thyratron. The device has been designated HY-5505. The tube has a calculated inductance well below 100 nH, and its operation is expected to provide considerable information concerning the commutation and holdoff characteristics of low inductance, multigap thyratrons.

-62-

existing design will work sufficiently well so that we can address the important matter of anode dissipation. The existing design obviously does not address this consideration, and we expect to operate the tube only at low prr.

c. Details of the Design

Cathode

A standard EG&G Type HY-5 cathode is used. This cathode has an area of 500 cm^2 and is normally rated at 5 kA. Such cathodes have delivered 9 to 10 kA for pulse widths of 10 to 20 µS at an average current of 30 A. The smaller 1802-type cathode (100 cm^2) normally rated at 1.5 kA has operated at 14 kA for pulse widths of 50 nS at low pulse repetition rates. For a given cathode, the maximum allowable current density at the tips of the cathode vanes increases as the square root of the current, while the current density for cathode arcing increases inversely with the cube root of the pulse width. From the experimental data and the known scaling relations for cathode performance, it is likely that the HY-5 cathode can deliver a few tens of kilo-amperes for the pulse widths applicable to this Program (less than 100 nS). We therefore concluded that the HY-5 cathode was a good choice for this experimental tube, particularly since the tube's holdoff and commutation characteristics are our primary concerns.

Reservoir

The tube has a high-capacity reservoir of the type used in EG&G's HY-53. The tube will be filled with deuterium to a pressure of 400 microns at the standard reservoir voltage setting, and a pressure-voltage calibration curve will be established before pinch-off. During operation, the input power to the reservoir will be adjustable and regulated. An operating pressure range of 200 to 600 microns is anticipated.

Auxiliary Grid

The tube is equipped with an auxiliary grid (also serves as a cathode baffle), the normal function of which is to reduce jitter and anode delay time. We have found with tetrode tubes that when negative control grid bias

is used, and the auxiliary grid is used to trigger the tube, significant increases in the tube's di/dt capability result thereby.

Control and Gradient Grids

These grids are the most critical of the tube's elements. They provide capacitance-controlled distribution of the anode voltage over the length of the tube, with no biasing circuit being used. The control grid is baffled in the usual fashion, and the various apertures of the gradient grids are offset therefrom and throughout the tube's structure such that no line of sight exists among the various grids. This arrangement is expected to provide maximum holdoff at the expense of triggerability at low epy, a reasonable concession for this tube. A representative gradient grid (with its ceramic spacers) is shown in Figure 28.

The grid apertures, of course, present the minimum cross-sectional area to the discharge. For the grids having the smaller set of annular radii (and hence the minimum area), the total aperture area is 1.14 $inch^2$. At normal thyratron operating pressure (300 microns) and pulse widths (5 to 10 μS), this area would give rise to grid-quenching (self-interruption) of the discharge at about ib = 10,000 A. Due, however, to the inertia of the pertinent gas dynamic processes, the capability of a constricted area to pass high current discharges increases markedly as the pulse width decreases. Quenching has not been observed for pulse widths less than about 1 μS, and is not expected to be a factor in the operation of this tube, even for the relatively thick grid structures employed.

The aperture offset-to-width ratio was chosen to be consistent with that of existing and proven tube designs. The effects on tube operation of this parameter (as a function of E-E spacing) are not clear, and theoretical investigations are now being performed in this area.

On the reasonable assumption that the gap comprised by the anode and the last gradient grid will be the last to fire during the cascading process, the last insulator has been made materially longer than all other insulators exposed to high voltages. As a result, the upper gradient grid is equipped with a shield to equalize the voltage gradient along the insulator's length.
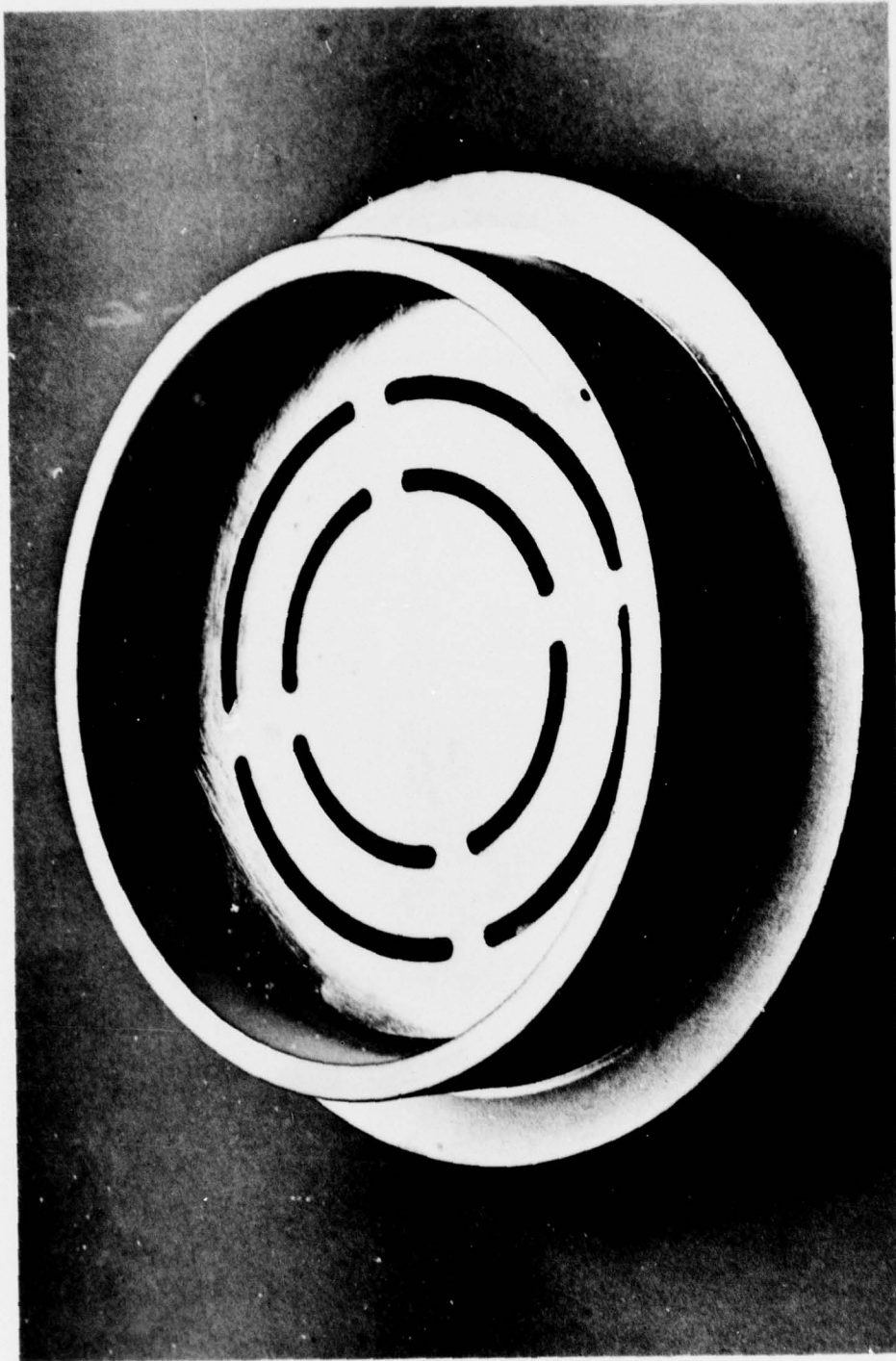
-64-

Figure 28. Typical gradient grid and ceramic insulator assembly. Note the annular grid slots. For a given stage, the slots in the two grid-halves are in line. From stage-to-stage, the slots are offset (refer to Figure 27).

Anode

The actual anode is a molybdenum disc, 0.060 inch thick, supported by the anode cup. No provision has been made for active cooling of the anode in this design since anode heating is a matter requiring extensive investigation, and is therefore beyond the scope of the immediate investigation.

The anode cup has been fitted with a stud merely for experimental convenience. For minimum inductance, one would make connections to the anode at the outer reaches of the anode cup flange. The anode cup and gradient grid flanges will be fitted with appropriate guard rings (not shown in Figure 27).

7.0 PRINCIPAL CONCLUSIONS AND PLAN FOR FUTURE WORK

a. Principal Conclusions

Several conclusions relative to the design of high voltage, low inductance hydrogen thyratrons can be drawn from the work of Phase I. First, it is highly probable that tube inductance (and not commutation time) will limit the maximum rate of rise of anode current. It thus follows that the emphasis of our continuing work should be placed on the control of those factors that influence tube inductance as opposed to the study of phenomena related to the propagation of the hydrogen discharge.

The inductance of any device is intrinsically related to its physical dimensions, and the inductance is decreased as those dimensions are decreased. On the other hand, the smaller the dimensions, the worse the problems associated with high voltage insulation. Hence the conflict between high voltage and low inductance.

For the regime of inductance and voltage applicable to this Program, we stand at the very limit of a possible compromise between inductance and voltage. On the basis of the inherent characteristics of hydrogen thyratrons, we conclude that a satisfactory compromise can be struck, but this conclusion is subject to the practical limitations imposed by the breakdown characteristics of the ceramic insulators that are universally used in the construction of high power tubes.

For a pulse of anode current 60 nS wide, we consider a peak current of the order of 40 kA with a rise time of the order of 20 nS to be a realistic goal. At shorter rise times, thyratron operation is dominated by the commutation time, and it is not clear that any efforts to reduce the commutation time would meet with success. For the range of tube inductance that we feel is ultimately achievable for a 250 kV thyratron (40-80 nH), 40 kA is a reasonable peak current such that the inductive drop across the tube is not excessively high. Forty kiloamperes for 60 nS is also consistent with a short, low inductance cathode.

-67-

These performance estimates are first contingent on two principal and, as yet, unproven assumptions. The first of these is that a multigap tube of the general design discussed in Section 6 is capable of holding off (and recovering to) 250 kV, and can also be made to commutate as an ordinary thyratron. We expect commutation, but we are less sure (although not pessimistic) about holdoff and recovery.

The second assumption is that ceramic insulators typically of the lengths shown in Section 6 can in fact withstand the stresses imposed upon them during charging and commutation. This can be established only by experimental investigation as discussed in Section 4h. If the insulators fail, it appears that a sacrifice in tube inductance will be necessary to gain insulator length, or some new and as yet unconsidered geometry will need to be developed.

There are second-order effects that could affect the performance of a multigap tube operated at high di/dt. These include discharge propagation effects in the upper sections (with beam formation a possibility), cathode arcing, arbitrary gap breakdown, and grid quenching at lower than usual limits for tubes operated at very high plate breakdown factors. Such phenomena are in general too complicated to analyze theoretically, and experimental work is again required.

b. Plan for Future Work

Before developing a detailed work plan for Phase II, it is first necessary for us to determine if the tube of Section 6 operates as we expect, and also to determine the stress levels that the insulators can in fact withstand. Our first priorities are thus to test both the tube and the ceramic samples.

We plan to do further theoretical work in at least two areas. The first of these is to investigate the feasibility of altering the interelectrode capacitances of the various stages in such a way as to force a more favorable transient distribution of epy across the tube. This would allow us to better utilize the available space within the coaxial current return and thus lower the inductance of the tube, subject only to the breakdown strength of the insulating oil.

We also plan to investigate the holdoff-triggerability compromise by using field plotting techniques to investigate the effects of aperture width and offset as a function of E-E spacing. We feel that this is necessary to hedge against the holdoff problems that we expect to encounter at high epy.

Two important considerations relating to holdoff and commutation remain to be experimentally investigated. The first is the actual increase in gas breakdown voltage that can be achieved in practice under conditions of fast pulse charging as opposed to static or low frequency conditions (DGBV vs SBV). Clearly, the higher the ratio of the dynamic to static breakdown voltages, the fewer the number of sections required to hold off 250 kV, and the lower the tube inductance. During the course of our work under contract to LASL, we have successfully operated tubes nominally rated at 25 kV at voltages as high as 50 kV (and this at high tube pressure) under pulse charge conditions, and the HY-5505 as discussed in Section 6 must operate at over 50 kV per section if epy = 250 kV is to be achieved. It is clear that an accurate determination of DGBV/SBV (as a function of time) is essential to the development of high voltage, low inductance tubes.

The second area of concern is the time that the upper space can hold off essentially the full voltage epy as opposed to the time required for the upper stage to commutate. It is essential that commutation win the race, or an upper-stage arc is likely. Multistage tubes such as the HY-541/MAPS 250 have successfully operated in this regard, but the matter of upper stage holdoff time versus commutation time remains a matter of key concern in the operation of multigap tubes.

Regardless of how the first experimental tube and the ceramic samples perform, valuable experimentally generated information will be gained from their evaluation. A second generation tube, designed to operate at high pulse repetition rates, is now in the offing, with the completion of its design awaiting the information to which we have just alluded. The purpose of the second tube (after design modifications to correct for such deficiencies as

may be revealed by the operation of the first tube at high epy) is to provide essentially trouble-free operation at high epy, high di/dt, and high pulse repetition rates. This will enable us to gain insight into the performance of multigap tubes at high di/dt and high pulse repetition rates. Again, the emphasis is on letting the tube tell us where the problems are.

The exact course of the theoretical and experimental work during Phase II will of necessity be guided by experimentally obtained results.

8.0 REFERENCES

1. Corson, D., and Lorrain, P., _Introduction to Electromagnetic Fields and Waves_, Freeman and Co., San Francisco, 1962. P. 246.

2. Kraus, John D., _Electromagnetics_, McGraw-Hill, New York, 1953. P. 74.

3. Alston, L.L. (Editor), _High Voltage Technology_, Oxford University Press, London, 1968. P. 6.

4. Kohl, Walter H., _Handbook of Materials and Techniques for Vacuum Devices_, Reinhold Publishing Corporation, New York, 1967. P. 583.

APPENDIX 1

MATHEMATICAL MODEL FOR HYDROGEN THYRATRON
AND DERIVATION OF CIRCUIT EQUATIONS

Assume that during commutation, the anode potential, $e(t)$, of a hydrogen thyratron attempts to decrease at an exponentially increasing rate with a time constant, τ_i, depending only on the hydrogen pressure such that $e(t) = V_0$ $(2-\varepsilon^{t/\tau_i})$ where V_0 is the initial anode potential. For purposes of circuit analysis, $e(t)$ may be considered as a voltage source acting in opposition to that in series with the transmission line or energy storage capacitor being switched by the thyratron. Note that $e(t) = V_0$ at $t = 0$, and at $t = \tau_i \ln 2$ (defined as $t = T$), $e(t) = 0$. The steady-state tube drop is ignored.

Two energy storage mechanisms may be considered for the circuit external to the thyratron. The first (Case 1) is a long, charged transmission line of characteristic impedance, Z_0, and total capacitance, C, such that the two-way travel time is $2Z_0C$. The second (Case 2) is a charged energy storage capacitor, C.

Assume that both circuits operate with an equivalent series inductance, L, which includes that of the thyratron, L_T (but not that of the line for Case 1), and an equivalent series resistance, R (which for Case 1 includes Z_0). The waveform of $e(t)$ and the two circuits under consideration in both the time and frequency domains are shown in Figure A-1. The task is to derive analytical solutions for the circuit current, $i(t)$, its derivative, di/dt, and the actual thyratron anode voltage, $e(b)$, where $e(b) = e(t) + L_T \, di/dt$ for the circuits of Figure A-1(b) and A-1(c). Solutions are required both during commutation $[e(t) \neq 0]$ and subsequent thereto $[e(t) = 0]$.
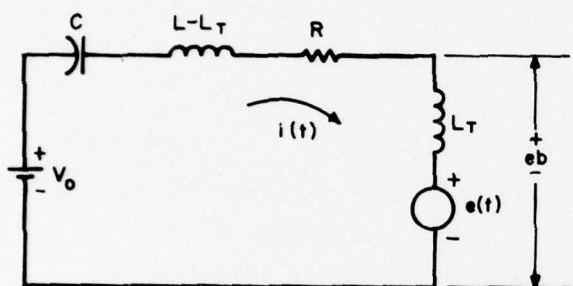
A-1
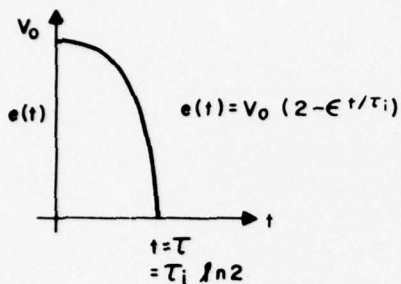
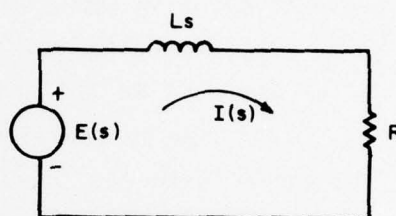(a) Waveform of the voltage source, $e(t)$. $e(t)$ is defined as zero for $t > T$. Steady-state tube drop is ignored.

$$e(t) = V_0 (2 - \epsilon^{t/\tau_i})$$

$$t = \tau = \tau_i \ln 2$$
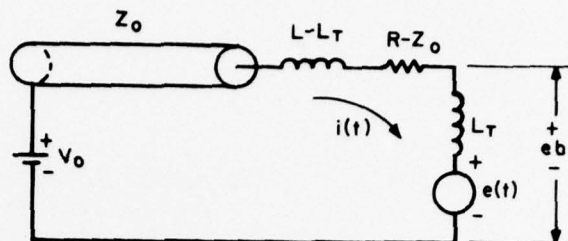
(b) Time domain circuit for Case 1 (Long Transmission Line).

(c) Time domain circuit for Case 2 (Energy Storage Capacitor).

(d) Frequency domain circuit and basic Laplace equation for current during commutation — Case 1. The voltage $E(s)$ is the Laplace Transformation of the net voltage causing $i(t)$ to flow.
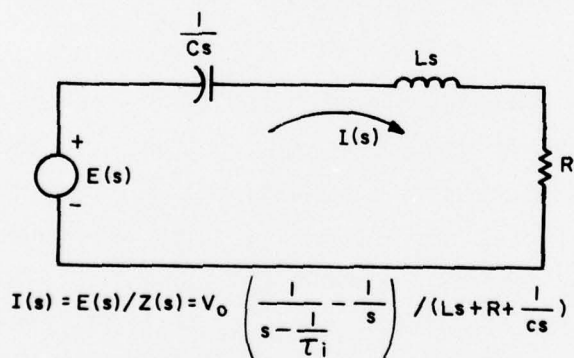
$$I(s) = E(s)/Z(s) = V_0 \left(\frac{1}{s - \frac{1}{\tau_i}} - \frac{1}{s} \right) / (Ls + R)$$

(e) Frequency domain circuit and basic Laplace equation for current during commutation — Case 2.

$$I(s) = E(s)/Z(s) = V_0 \left(\frac{1}{s - \frac{1}{\tau_i}} - \frac{1}{s} \right) / (Ls + R + \frac{1}{cs})$$

Figure A-1. Assumed thyratron behavior with circuit models and equations used to derive analytical solutions for thyratron and circuit operation under conditions where commutation of thyratron cannot be ignored.

Case 1. Long Transmission Line

Here we assume that the line is sufficiently long so that it looks like a voltage source in series with Z_0 until the circuit current is asymptotically reaching its maximum value. This requires that $2Z_0C \geq T + 5L/R \equiv T + 5T_L$. The basic Laplace equation for the circuit current is given in Figure A-1(d) and it is a straightforward matter to solve for the current $i(t)$ during the commutation interval. The differentiation of $i(t)$ yields di/dt directly, and the thyratron anode voltage, eb, is then readily obtained. The results of these operations yield the following expressions which are valid during the commutation interval ($0 \leq t \leq T$):

$$i(t) = \frac{V_0}{R} \left[K_A \varepsilon^{t/\tau_i} + (1-K_A)\varepsilon^{-t/\tau_L} - 1 \right]$$

$$\frac{di}{dt} = \frac{V_0}{L} \left[(1-K_A)(\varepsilon^{t/\tau_i} - \varepsilon^{-t/\tau_L}) \right]$$

$$eb = V_0 \left[2 - (1-K_B)\varepsilon^{t/\tau_i} - K_B\varepsilon^{-t/\tau_L} \right]$$

where

$$K_A = \tau_i/(\tau_i + \tau_L)$$

$$K_B = K_C(1-K_A) \text{ and } K_C = L_T/L$$

and

$$\tau_L = L/R$$

as before.

For the post-commutation period $(T < t < 2Z_0C)$, the voltage $e(t)$ is zero. The expression for the circuit current may then be determined by evaluating the above expression for $i(t)$ at $t = T$ (thus finding the energy stored in the circuit inductance), and deriving a new expression for $i(t)$ based on the energy storages then present in the system. The expressions for di/dt and eb can then be derived as before. The results are:

$$i(t) = \frac{V_0}{R} \left[1-(1-K_D) \, \varepsilon^{-(t-T)/\tau_L} \right]$$

$$\frac{di}{dt} = \frac{V_0}{L} \left[(1-K_D) \, \varepsilon^{-(t-T)/\tau_L} \right]$$

$$eb = K_C V_0 \left[(1-K_D) \, \varepsilon^{-(t-T)/\tau_L} \right]$$

where $K_D = K_A - (1-K_A)(1-\varepsilon^{-K_E})$ and $K_E = (\tau_i/\tau_L) \ln 2$ and K_A and τ_L are as defined before.

Case 2. Energy Storage Capacitor

The procedure here is essentially the same as that for Case 1, except that it is necessary to determine the energies stored in both the circuit inductance and the storage capacitor at $t = T$ before proceeding with the post-commutation solution. We have addressed Case 2 only for the situation where $4/LC > (R/L)^2$, i.e., for conditions where the circuit response is oscillatory. This is, of course, the case of greatest interest.

For $0 \leq t \leq T$,

$$i(t) = \frac{V_0}{L} \frac{(\gamma - \alpha)}{(\beta^2 + \gamma^2)} \, \varepsilon^{-\alpha t} (\varepsilon^{\gamma t} - \cos\beta t - \frac{\gamma}{\beta} \sin\beta t)$$

A-4

$$\frac{di}{dt} = \frac{V_0}{L} \frac{(\gamma - \alpha)^2}{(\beta^2 + \gamma^2)} \varepsilon^{-\alpha t} (\varepsilon^{\gamma t} - \cos\beta t + \delta \sin\beta t)$$

$$eb = V_0 \left[2 - \varepsilon^{(\gamma - \alpha)t} + \frac{L_T}{L} \frac{(\gamma - \alpha)^2}{(\beta^2 + \gamma^2)} \varepsilon^{-\alpha t} (\varepsilon^{\gamma t} - \cos\beta t + \delta \sin\beta t) \right]$$

where

$$\alpha = R/(2L)$$
$$\beta = \left\{ [1/(LC)] - \alpha^2 \right\}^{1/2}$$
$$\gamma = \alpha + 1/\tau_i$$
$$\delta = \frac{\beta^2 + \alpha\gamma}{\beta(\gamma - \alpha)}$$

To determine the energy storages at $t = T$, one first evaluates the above expression for $i(t)$ at $t = T$. This yields

$$I_0 = \frac{V_0}{L} \frac{(\gamma - \alpha)}{(\beta^2 + \gamma^2)} \varepsilon^{-\alpha t} (\varepsilon^{\gamma T} - \cos\beta T - \frac{\gamma}{\beta} \sin\beta T) \ .$$

By evaluating di/dt at $t = T$, the voltage drop $L\,di/dt$ is found. The drop across the resistor is $I_0 R$. The voltage $e(t)$ is zero, and the voltage then present on the storage capacitor is readily determined by Kirchhoff's law to be

$$E_0 = V_0 \frac{(\gamma^2 - \alpha^2)}{(\beta^2 + \gamma^2)} \varepsilon^{-\alpha T} (\varepsilon^{\gamma T} - \cos\beta T + \eta \sin\beta T)$$

where

$$\eta = \frac{\beta^2 - \alpha\gamma}{\beta(\gamma + \alpha)} \ .$$

A-5

It then follows that for $t > T$

$$i(t) = \frac{E_0}{\beta L} \varepsilon^{-\alpha(t-T)} \sin[\beta(t-T)] + \frac{I_0}{\theta} \varepsilon^{-\alpha(t-T)} \cos[\beta(t-T) + \cos^{-1}\theta]$$

$$\frac{di}{dt} = \varepsilon^{-\alpha(t-T)} \left\{ \frac{E_0}{\beta L} \left\{ \beta\cos[\beta(t-T)] - \alpha\sin\beta[t-T] \right\} - \frac{I_0}{\theta} \left\{ \beta\sin[\beta(t-T) \right. \right.$$

$$\left. \left. + \cos^{-1}\theta] + \alpha\cos[\beta(t-T) + \cos^{-1}\theta] \right\} \right\}$$

$$e_b = \frac{L_T}{L} E_0 \varepsilon^{-\alpha(t-T)} \left\{ \cos[\beta(t-T)] - \frac{\alpha}{\beta} \sin[\beta(t-T)] \right\}$$

$$- L_T I_0 \frac{\beta}{\theta} \varepsilon^{-\alpha(t-T)} \left\{ \sin[\beta(t-T) + \cos^{-1}\theta] + \frac{\alpha}{\beta} \cos[\beta(t-T) + \cos^{-1}\theta] \right\}$$

where $\theta = \beta(\beta^2 + \alpha^2)^{-1/2}$.

In general, the peak current occurs after commutation. The time of the peak current can be determined by setting the post-commutation expression for di/dt equal to zero and solving for $t = t_{peak}$. The magnitude of the peak can then be determined by evaluating the post-commutation expression for $i(t)$ at $t = t_{peak}$.

Figure A-2 shows a comparison of the actual anode current of a hydrogen thyratron operated at high di/dt and the anode current as calculated using the equations developed for Case 2. The model predicts with reasonable accuracy the overall shape of the current pulse, including the early exponential rise, the peak and the time of the peak, and the pulse width.

The model accurately predicts the increase in anode fall time for tubes operated at high di/dt, and also the extent to which the thyratron inductance controls discharge circuit performance.
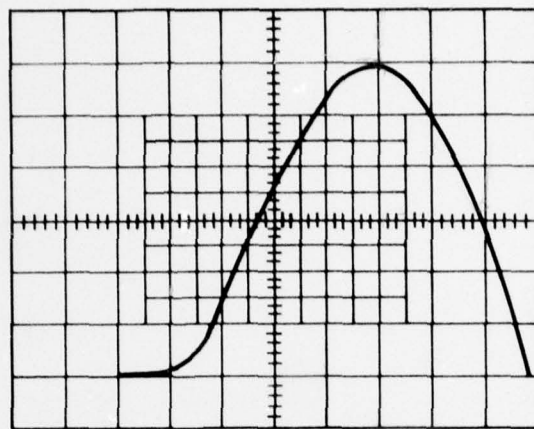
ACTUAL ANODE CURRENT
I KA/MAJ. DIV.; 10 NS/MAJ. DIV.
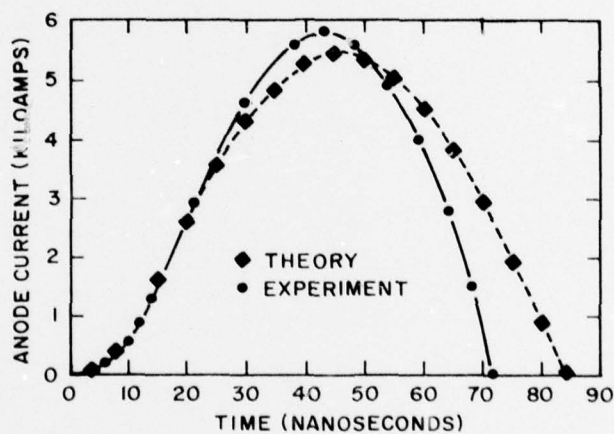
COMPARISON OF THEORY AND EXPERIMENT

TOTAL CIRCUIT INDUCTANCE	43.5 NH
TUBE INDUCTANCE	30 NH
STORAGE CAPACITANCE	13.5 NF
TUBE IONIZATION TIME CONSTANT	20 NS
$R_L = 0.05$ OHMS (CVR); ANODE VOLTAGE 10 KV	

Figure A-2. Comparison of theory and experiment showing that the theoretical model predicts the anode current pulse.

DISTRIBUTION LIST

012   Defense Documentation Center
ATTN: DDC-TCA
Cameron Station (Bldg 5)
Alexandria, VA 22314

001   Code R123, Tech Library
DCA Defense Comm Engrg Ctr
1800 Wiehle Ave
Reston, VA 22090

001   Defense Communications Agency
Technical Library Center
Code 205 (P.A. Tolovi)
Washington, DC 20305

001   Office of Naval Research
Code 427
Arlington, VA 22217

001   Commander
Naval Surface Weapons Center
ATTN: F-12 (K. Baile)
Dahlgren, VA 22448

001   Cdr, Naval Surface Weapons Center
White Oak Laboratory
ATTN: Library Code WX 21
Silver Spring, MD 20910

001   Commander
Naval Surface Weapons Center
ATTN: Dr. M. F. Rose
Dahlgren, VA 22448

001   Commander
Naval Surface Weapons Center
ATTN: Dr. Gripshover
Dahlgren, VA 22448

001   Commander
Naval Surface Weapons Center
ATTN: F-12 (D. Lindberg)
Dahlgren, VA 22448

001   Command, Control & Communications
Division
Development Center
Marine Corps Develop & Educ Comd
Quantico, VA 22134

001   Rome Air Development Center
ATTN: Documents Library (TILD)
Griffiss AFB, NY 13441

001   HQ, Air Force Systems Command
ATTN: DLCA
Andrews AFB
Washington, DC 20331

001   Cdr, MIRADCOM
Redstone Scientific Info Center
ATTN: Ch, Document Section
Redstone Arsenal, AL 35809

001   Commandant
US Army Aviation Center
ATTN: ATZQ-D-MA
Fort Rucker, AL 36362

001   Director, Ballistic Missile Defense
Advanced Technology Center
ATTN: ATC-R, PO Box 1500
Huntsville, AL 35807

001   Commander
US Army Intelligence Center &
School
ATTN: ATSI-CD-MD
Fort Huachuca, AZ 85613

001   Commander
HQ, Fort Huachuca
ATTN: Technical Reference Div
Fort Huachuca, AZ 85613

001   Commander
Naval Surface Weapons Center
ATTN: F-12 (H. Odom)
Dahlgren, VA 22448

001 Cdr, US Army Research Office
ATTN: DRXRO-IP
PO Box 12211
Research Triangle Park, NC 27709

001 Cdr, US Army Research Office
ATTN: DRXRO-PH (Dr. R. Lontz)
PO Box 12211
Research Triangle Park, NC 27709

001 Commandant
US Army Inst for Military Assistance
ATTN: ATSU-CTD-MO
Fort Bragg, NC 28307

001 Commandant
US Army Air Defense School
ATTN: ATSA-CD-MC
Fort Bliss, TX 79916

001 Commander
US Army Nuclear & Chemical Agency
7500 Backlick Rd, Bldg 2073
Springfield, VA 22150

001 HQ, TCATA
Technical Information Center
ATTN: Mrs. Ruth Reynolds
Fort Hood, TX 76544

001 Commander, DARCOM
ATTN: DRCDE
5001 Eisenhower Ave
Alexandria, VA 22333

001 Cdr, US Army Signals Warfare Lab
ATTN: DELSW-OS
Vint Hill Farms Station
Warrenton, VA 22186

001 Commander
US Army Mobility Equip R&D Command
ATTN: DRDME-R
Fort Belvoir, VA 22060

001 Maxwell Laboratories
ATTN: Mr. R. Fitch
9244 Balboa Ave
San Diego, CA 92123

002 Commander
US Army Logistics Center
ATTN: ATCL-MC
Fort Lee, VA 22801

001 Cdr, PM Concept Analysis Center
ATTN: DRCPM-CAC
Arlington Hall Station
Arlington, VA 22212

001 Chief
Ofc of Missile Electronic Warfare
Electronic Warfare Lab, ERADCOM
White Sands Missile Range, NM 88002

001 Chief
Intel Materiel Dev & Support Ofc
Electronic Warfare Lab, ERADCOM
Fort Meade, MD 20755

001 Cdr, Harry Diamond Labs
ATTN: DELHD-CO
2800 Powder Mill Road
Adelphi, MD 20783

001 Commander
ARRADCOM
DRDAR-TSB-S
Aberdeen Proving Ground, MD 21005

001 Commander, ERADCOM
ATTN: DRDEL-CG; -CD; -CS (IN TURN)
2800 Powder Mill Road
Adelphi, MD 20783

001 Cdr, ERADCOM
ATTN: DRDEL-CT
2800 Powder Mill Road
Adelphi, MD 20783

001 Dr. John Hammond
W. J. Schafer Associates, Inc.
Clinton Bldg, Suite 408
2109 W. Clinton Avenue
Huntsville, AL 35805

001 Cdr, Air Force Weapons Laboratory
AFWL/ALE (J. O'Loughlin)
Kirtland Air Force Base
New Mexico 87117

001   Cdr, ERADCOM
     ATTN: DRDEL-PAO
     2800 Powder Mill Road
     Adelphi, MD 20783

001   Cdr, ERADCOM
     ATTN: DRDEL-LL; -SB; -AP (IN TURN)
     2800 Powder Mill Road
     Adelphi, MD 20783

001   Cdr, ERADCOM
     ATTN: DRDEL-AQ
     2800 Powder Mill Road
     Adelphi, MD 20783

001   Cdr, ERADCOM
     ATTN: DRDEL-PA; -ILS; -ED (IN TURN)
     2800 Powder Mill Road
     Adelphi, MD 20783

001   HQ, Harry Diamond Laboratories
     ATTN: DELHD-TD (Dr. W.W. Carter)
     2800 Powder Mill Road
     Adelphi, MD 20783

     Commander
     US Army Electronics R&D Command
     Fort Monmouth, NJ 07703

       1   DELET-D
       1   DELET-DD
       2   DELET-DT
       5   DELET-BG
       1   DELSD-L (Tech Library)
       2   DELSD-L-S (STINFO)

     Commander
     US Army Communications R&D Command
     Fort Monmouth, NJ 07703

       1   DRDCOM-COM-RD
       1   USMC-LNO
       1   ATFE-LO-EC

001   Cdr, Air Force Weapons Laboratory
     ATTN: Dr. A. Guenther (AFWL/CA)
     Kirtland Air Force Base, NM 87117

001   Lawrence Livermore Laboratory
     ATTN: L. Reginato
     PO Box 808
     Livermore, CA 94550

     Commander
     US Army Communications & Electronics
     Materiel Readiness Command
     Fort Monmouth, NJ 07703

       1   DRSEL-PL-ST
       1   DRSEL-MA-MP
       2   DRSEL-PA

001   CINDAS
     Purdue Industrial Research Park
     2595 Yeager Road
     W. Lafayette, IN 47096

002   MIT- Lincoln Laboratory
     ATTN: LIBRARY (Rm A-082)
     PO Box 73
     Lexington, MA 02173

001   NASA Scientific & Tech Info Facility
     Baltimore/Washington Intl Airport
     PO Box 8757, MD 21240

001   National Bureau of Standards
     Bldg 225, Rm A-331
     ATTN: Mr. Leedy
     Washington, DC 20231

002   Advisory Group on Electron Devices
     201 Varick Street, 9th Floor
     New York, NY 10014

002   Advisory Group on Electron Devices
     ATTN: SECY, Working Grp D (Lasers)
     201 Varick Street
     New York, NY 10014

001   TACTEC
     Battelle Memorial Institute
     505 King Avenue
     Columbus, OH 43201

001   Plastics Tech Eval Center
     Picatinny Arsenal, Bldg 176
     ATTN: Mr. A.M. Anzalone
     Dover, NJ 07801

001   Metals & Ceramics Inf Center
     Battelle Memorial Institute
     505 King Avenue
     Columbus, OH 43201

001   Mr. Phil Mace
        Los Alamos Scientific Laboratory
        PO Box 1663
        Los Alamos, NM   87545

001   Cdr, Defense Advanced Research
        Project Agency
        DARPA/STO (J. Mangano)
        1400 Wilson Boulevard
        Arlington, VA   22209

001   Avco-Everett Research Laboratory
        2385 Revere Beach Parkway
        ATTN: Mr. R. Feinberg
        Everett, MA   02149